

1 **An experimental determination of the liquidus and a thermodynamic melt model**
2 **in the CaCO₃-MgCO₃ binary, and modelling of carbonated mantle melting**

3 Sutao Zhao^a, Stefano Poli^{b*}, Max W. Schmidt^c, Michele Rinaldi^{b+}, Simone Tumiami^b

4

5 a. Institute of Geophysics & Geomatics and Subsurface Multi-scale Imaging Lab
6 (SMIL), State Key Laboratory of Geological Processes and Mineral Resources,
7 China University of Geosciences, Wuhan, 430074, China. sky_zst@163.com

8 b. Dipartimento di Scienze della Terra, Università degli Studi di Milano, Via Botticelli
9 23, Milano 20133, Italy. stefano.poli@unimi.it, simone.tumiati@unimi.it

10 c. Department of Earth Sciences, ETH, Clausiusstrasse 25, CH-8092 Zürich,
11 Switzerland. max.schmidt@erdw.ethz.ch

12 * Corresponding author: E-mail address: stefano.poli@unimi.it (Stefano Poli).

13 † now at School of Earth & Environmental Sciences, The University of St Andrews,
14 Scotland, United Kingdom, mr267@st-andrews.ac.uk

15

16

17 **ABSTRACT**

18 The binary CaCO₃-MgCO₃ constitutes the reference model system to reconstruct the
19 petrogenesis of carbonated rocks, and of carbonatite magmas possibly generated in the

20 Earth's mantle. We experimentally determined the melting of aragonite and magnesite
21 to pressures of 12 GPa, and of calcite-magnesite mixtures at 3 and 4.5 GPa, at variable
22 Ca/(Mg+Ca) (X_{Ca}). The melting curves of aragonite, and magnesite have similar slopes,
23 the latter melting ≈ 30 °C higher than aragonite. In the Ca-Mg binary, the minimum of
24 the liquidus surface situates at an X_{Ca} of 0.65-0.60, at 1200 °C - 3 GPa, and 1275 °C -
25 4.5 GPa. Together with available data at 1 and 6 GPa, the minimum liquid composition
26 remains approximately constant with pressure. All available experimental data are then
27 fit by the first thermodynamic model for CaCO_3 - MgCO_3 liquids. Surprisingly, although
28 carbonate liquids should behave as relatively simple molten salts, the liquids display
29 large non-ideality and a three-component, pressure dependent, asymmetric liquid
30 solution model is required to model the liquidus surface. Attempts to use only the two
31 end-member components fail, invariably generating a very wide magnesite-liquid loop
32 in disagreement with the experimental evidence.

33 The liquid model is then used to evaluate results of experimentally determined phase
34 relationships for carbonated peridotites in $\text{CaO-MgO-SiO}_2\text{-CO}_2$ (CMS- CO_2), and CaO-
35 $\text{MgO-Al}_2\text{O}_3\text{-SiO}_2\text{-CO}_2$ (CMAS- CO_2). Computations highlight that the liquid
36 composition formed in a model carbonated mantle do not represent "minimum melts"
37 but are more magnesian at high pressure. The pressure-temperature position of the
38 solidus, as well as its dP/dT slope, including the appearance or absence of the
39 "carbonatite ledge", depend on bulk composition, unless truly invariant assemblages
40 occur.

41

42 **1. INTRODUCTION**

43 Carbonatitic liquids are stable in a variety of tectonic settings, in the deep upper mantle
44 and transition zone (Dasgupta and Hirschmann, 2006; Rohrbach and Schmidt, 2011),
45 in subcontinental mantle (Yaxley et al., 2022), at the oceanic asthenosphere-lithosphere
46 boundary (Gaillard et al. 2008), along the slab-mantle interface in warm subduction
47 zones (Poli, 2015), but mostly arise near the surface through differentiation and
48 immiscibility of alkaline magmas (Mitchell, 2005), leading to deposits of critical
49 elements (REE, Chakhmouradian and Zaitsev, 2012). Furthermore, carbonatites sensu
50 lato are suspected to initiate melting in plumes (Hofmann et al., 2011; Stagno et al.,
51 2013), and sometimes carbonatites occur with kimberlites, but their relation is heavily
52 debated (Russell et al. 2012 vs. Stamm and Schmidt, 2017). Because of their peculiar
53 physical properties (low viscosity, high electrical conductivity, Jones et al., 2013;
54 Gaillard et al., 2008), even small volume fractions of carbonatitic liquid have profound
55 effects on the dynamics of the Earth interior. Carbonatitic liquids play a fundamental
56 role in the deep carbon cycle, being extremely mobile and reactive compared to other
57 carbon compounds. Redox "freezing" of carbonatitic liquids is responsible for the
58 precipitation of diamonds in the deeper upper mantle (Rohrbach and Schmidt, 2011;
59 Timmerman et al., 2021).

60 Calcite and dolomite are the dominant carbonates crystallizing from carbonatitic
61 magmas (Mitchell, 2005), and dolomite and magnesite are the carbonates most

62 commonly stable in high-pressure carbonated eclogites and peridotites (e.g. Wyllie and
63 Huang, 1975; Dasgupta et al., 2005; Poli et al. 2009). As a consequence the model
64 binary system $\text{CaCO}_3\text{-MgCO}_3$ has been extensively used as a basis to predict phase
65 relationships in more complex systems, approaching natural compositions. Dasgupta et
66 al. (2005) showed that solidus temperatures increase with increasing $\text{Ca}/(\text{Ca}+\text{Mg})$ of
67 the bulk, owing to the strong influence of the $\text{CaCO}_3\text{-MgCO}_3$ binary liquidus surface
68 on the solidus of carbonate bearing eclogite. In peridotitic systems, Dalton and Presnall
69 (1998a), and Dasgupta and Hirschmann (2007a) demonstrated that near-solidus
70 carbonatite derived from mantle lherzolite becomes less calcic with increasing pressure,
71 as a result of the pressure dependence of $\text{CaCO}_3\text{-MgCO}_3$ liquidus surface. A robust
72 thermodynamic analysis of the binary system is therefore of the utmost importance for
73 the interpretation of phase relationships in natural compositions.

74 High pressure melting of CaCO_3 (Fig 1a) was investigated by Irving and Wyllie (1975),
75 Suito et al. (2001), Spivak et al. (2012), Li et al. (2017), Shatskiy et al. (2018), and
76 Zhao et al. (2019). Despite up to 100 °C differences in the temperature of melting, in
77 part related to experimental uncertainties and to procedures used, the different
78 determinations of the dP/dT slope up to 6 GPa are somewhat consistent. On the contrary,
79 at 6-15 GPa, experimental results by Li et al. (2017) may be interpreted as suggesting
80 a change in the sign of dP/dT slope of the melting curve, from positive to negative
81 ("backbend"), which largely differs from Spivak et al. (2012), and contrasts with
82 melting behaviour in other carbonates, e.g. MgCO_3 (Katsura and Ito, 1990), and FeCO_3
83 (Kang et al. 2015). Consequent differences in melting temperature amount to more than

84 200 °C at 14 GPa.

85 Melting of MgCO₃ (Fig. 1b) was constrained by Irving and Wyllie (1975), Katsura and
86 Ito (1990), Solopova et al. (2015), Mueller et al. (2017), and Shatskiy et al. (2018);
87 these studies are within expected experimental uncertainties mostly consistent,
88 although determinations by Müller et al. (2017) and Shatskiy et al. (2018) suggest
89 melting at temperatures lower than found in Katsura and Ito (1990).

90 Irving and Wyllie (1975), Huang and Wyllie (1976) and Byrnes and Wyllie (1981)
91 experimentally determined melting relations in the (pseudo-)binary CaCO₃-MgCO₃,
92 using piston cylinders (2.7 and 1.0 GPa). Buob et al. (2006), Müller et al (2017) and
93 Shatskiy et al (2018) focused on melting at 6 GPa by means of multi-anvil machines,
94 the latter study including a section at 3.0 GPa (Fig. 2). Four additional experiments at
95 6 GPa were performed by Sieber et al. (2020). Major discrepancies among these studies
96 concern differences in temperature and composition of the minimum of the liquidus
97 surface. At 2.7-3.0 GPa, the minimum was located at 1225 °C by Shatskiy et al. (2018),
98 approximately 60-70 °C lower than by Irving and Wyllie (1975). At 6 GPa the minimum
99 as determined by Shatskiy et al. (2018) is 50 °C higher than in Buob et al. (2006) and
100 more than 100 °C higher than in Müller et al. (2017), the experiments by Sieber et al.
101 (2020) grossly consistent with the liquidus surface proposed by Müller et al. (2017).
102 Notably, at 1 GPa, the minimum is located at $X_{Ca} = 0.67$ ($X_{Ca} = Ca/(Mg+Ca)$ molar
103 fraction) according to Byrnes and Wyllie (1981), at 3 GPa at $X_{Ca} = 0.53 - 0.58$,
104 according to Shatskiy et al. (2018) and Irving and Wyllie (1975) respectively, and at 6

105 GPa the minimum may vary from $X_{Ca} \sim 0.50$ (Buob et al. 2006), to 0.62 in Shatskiy et
106 al. (2018), to approx. 0.65 in Mueller et al. (2017). Very little information is available
107 on the location of the peritectic reaction dolomite = liquid + magnesite, and on the width
108 of the field Mg-rich dolomite + liquid.

109 Additionally, evidence of periclase on the liquidus surface at high pressure remains
110 ambiguous. Shatskiy et al. (2018) suggested an incongruent melting of magnesite both
111 at 3 and 6 GPa, and periclase was reported in Sieber et al. (2020) on the Mg-calcite side
112 of the liquidus. The occurrence of periclase would imply deviation of liquid
113 composition from the carbonate join. However, these studies do not provide topological
114 constraints to high pressure phase relationships bearing periclase, whose stability in the
115 binary is constrained by the reaction periclase + CO₂ = liquid (Fig. 1b).

116 Experiments in the model systems CaO-MgO-(Al₂O₃)-SiO₂-CO₂ (CMS-CO₂ and
117 CMAS-CO₂, Dalton and Presnall, 1998a, b; Gudfinnsson and Presnall, 2005; Luth,
118 2006; Keshav and Gudfinnsson, 2013; Novella et al., 2014) and in a wide range of bulk
119 compositions (e.g. Dasgupta et al., 2004; Yaxley and Brey, 2004; Dasgupta and
120 Hirschmann, 2010; Grassi and Schmidt, 2011; Poli, 2015) reveal that near solidus melts
121 of carbonated lithologies are commonly "dolomitic", i.e. carbonatitic, with X_{Ca} typically
122 in the range 0.5-0.7, up to $X_{Ca} = 0.8$ in hydrous systems (Hammouda, 2003; Poli, 2015),
123 underlining the importance of the location of this minimum in the binary.

124 A strong constrain for the thermodynamic analysis is the compositional width of the
125 liquidus - solidus loops. At 6 GPa, both Buob et al. (2006) and Müller et al. (2017)

126 obtained relatively tight loops (Fig. 2), notably on the Mg-side, leading to a much wider
127 liquid field compared to the geometry proposed by Shatskiy et al. (2018). The topology
128 of the phase diagram at 6 GPa is further complicated by the occurrence of aragonite on
129 the liquidus surface. Zhao et al. (2019) found the invariant point aragonite - calcite V -
130 liquid at approximately 5 GPa, 1670 °C, a P-T condition which is consistent with a
131 linear extrapolation of the boundary calcite I - aragonite as determined by Irving and
132 Wyllie (1975) and which predicts an aragonite+liquid field to occur at high pressures.
133 This field was found by Shatskiy et al. (2018) at 1650 °C, whereas aragonite was found
134 only to 1500 °C by Buob et al. (2006) (run ABU80/2), but not at 1600 °C. Müller et al.
135 (2017) on a bulk $X_{Ca} = 0.85$ did not observe phase transformations at 1575 and 1620 °C.
136 The aragonite + liquid field remains therefore poorly constrained.

137 Overall, very few run products were fully molten at conditions close to the minimum.
138 At 6 GPa there are only three experiments in the one phase liquid field in Buob et al.
139 (2006), three in Shatskiy et al. (2018) at 1500 °C, and none in Mueller et al. (2017).
140 Fully molten experiments are less affected by potential contaminants, notably hydrogen,
141 present or diffusing into the run charge, the system then deviating from the carbonate
142 binary. Also, it is commonly assumed that carbonate liquids follow a $M^{2+}CO_3$
143 stoichiometry (M = Ca, Mg, Fe), but there are no direct measurements of the M:C:O
144 ratios in the unquenchable liquids. Differences in experimental assemblies, e.g. varying
145 from welded noble metal capsules to open graphite containers may result in difference
146 in H₂O-, CO₂-, or C-content that could not be easily recognized.

147 In this work we close some gaps in the experimental melting relations of CaCO₃-
148 MgCO₃, in particular concerning the expected liquidus minima at 3 and 4.5 GPa and
149 provide the first thermodynamic model for carbonate liquids in this binary accounting
150 for the modifications in the shape of the liquidus surface with pressure. The solution
151 model is then applied to the melting of a carbonated mantle with an emphasis on
152 variations in the pressure temperature location of the solidus due to bulk composition.

153

154 **2. EXPERIMENTAL AND ANALYTICAL METHODS**

155 **2.1. Starting materials**

156 Starting mixtures were prepared from reagent-grade pure CaCO₃ powder (from
157 Merck) and pure natural magnesite collected from Eubea, Greece, with 0.01 a.p.f.u. Ca,
158 and iron content below detection limits for electron microprobe. Synthetic magnesite
159 was found too hygroscopic, in particular, complete drying of commercial magnesite is
160 only possible at temperatures where decarbonation begins. Mixtures were ground in
161 ethanol, dried at 200 °C and permanently stored at 110 °C in a vacuum oven to prevent
162 hydration.

163

164 **2.2. Experimental methods**

165 Experiments at pressures of 3.0 and 4.5 GPa, 1150 °C to 1500 °C, were conducted
166 in a 1000-ton Walker-type multi-anvil apparatus at the Università degli Studi di Milano
167 (UMI). A large volume 25/17 assembly was adopted to minimize thermal gradient in

168 the run charge, using Cr_2O_3 doped MgO-octahedra, and preformed pyrophyllite gaskets.
169 The assembly includes a ZrO_2 sleeve, graphite furnace, internal MgO spacers, and
170 molybdenum end spacers ensuring electrical contact. Temperature was controlled by
171 Eurotherm controllers within $\pm 2^\circ\text{C}$, and monitored by S-type ($\text{Pt}_{100}/\text{Pt}_{90}\text{Rh}_{10}$) axial
172 thermocouples. Temperature gradients are $<30^\circ\text{C}$ over the capsule length. Starting
173 materials were loaded into platinum capsules, initially 2 mm long. Two capsules at
174 different X_{Ca} ratio were packed axially in the central part of the furnace in order to verify
175 internal consistency of solidus/liquidus relationships. In order to reduce the influx of
176 hydrogen during the experiments, and ensure nearly-anhydrous run conditions, the
177 capsule was packed with Fe_2O_3 powder (Liu and O'Neill, 2004) into a MgO sleeve,
178 hematite efficiently reacting with any H_2 to magnetite and H_2O , which does not diffuse
179 through capsule walls. Additional information is available in Zhao et al. (2019).

180 Experiments at 6 and 12 GPa, and temperatures up to 2000°C were conducted in a
181 Walker-type multi-anvil at ETH Zurich, using assemblies composed of stepped 14/8
182 LaCrO_3 heaters, ZrO_2 sleeves, internal MgO spacers, and molybdenum end ring and
183 disc. Iridium capsules of 1.6 mm outer diameter were used above 1800°C as platinum
184 was found to melt at such temperatures.

185 In order to provide the internal consistency of results obtained in multi-anvil with
186 piston cylinder experiments, runs CCMS13 and P10-026, at 3.0 GPa, 1175°C and
187 1230°C , respectively, were performed in end-loaded piston cylinders at UMI and ETH,
188 using a salt-pyrex assembly.

189

190 **2.3. Analytical techniques**

191 After recovery, each capsule was mounted longitudinally in epoxy resin and
192 polished dry. After carbon coating, they were analyzed with a JEOL JXA8200 electron
193 microprobe (EPMA), equipped with five wavelength-dispersive spectrometers (WDS).
194 The quenched solids were measured at 15 kV acceleration voltage and 5 nA with a
195 defocused beam to minimize beam damage. Counting times were 30 s on the peak and
196 15 s on the background. Micro-Raman spectra were obtained with a Horiba LabRam
197 HR Evolution spectrometer equipped with a green solid-state laser (532 nm) focused
198 through a 100× objective available at the Università degli Studi di Milano. Experiments
199 in unary systems (pure magnesite or calcite) were imaged, blocky equilibrium crystals
200 with straight grain boundaries and 120° triple junctions can be unambiguously
201 distinguished from feathery quenched melt (see below).

202

203 **3. EXPERIMENTAL RESULTS**

204 40 successfully run experimental charges constitute the backbone of this study. Run
205 conditions and phase compositions are reported in the Table 1, representative
206 backscattered electron (BSE) images in Fig. 3.

207 Subsolidus run products are characterized by polygonal grains of a few tens of
208 micrometer size (Figs. 3a and b). Melts do not quench to glass and are detected by a
209 typical dendritic texture, resulting from the low viscosity of carbonate melts (Fig. 3c,

210 d). The boundary between melt and residual crystals is easily distinguishable, and
211 liquids always migrate to the hot point of the capsule, in this case the one closest to the
212 thermocouple (Fig. 3c, right side). A thin colloform layer of carbon at capsule walls,
213 approximately 1 μm thick, and sparse carbon “droplets” were sometimes observed, e.g.
214 at 3.0 GPa, 1350 $^{\circ}\text{C}$ likely from diffusion and related redox through the capsule walls,
215 pointing to a potential deviation of liquid composition from carbonate stoichiometry at
216 high pressures and temperatures. The amount of elemental carbon in any charge, as
217 determined by image analysis, is $< 1 \%$ and assumed to be negligible in the
218 thermodynamic analysis that follows.

219 Because of the existing discrepancies in the melting curves of CaCO_3 and MgCO_3 ,
220 we bracketed these curves at 12 GPa. Melting of CaCO_3 to pressures of 6 GPa was
221 constrained by experiments by Irving and Wyllie (1975), Suito (2001), Li et al. (2017),
222 and Zhao et al. (2019), yielding an overall coherent systematics (Fig. 1a), only Shatskiy
223 et al. (2018) obtained melting at 3 GPa at temperatures 80 $^{\circ}\text{C}$ lower than previous
224 studies (similar to their results on MgCO_3). Above 6 GPa, Li et al. (2017) suggest a
225 backbend of the solidus on the basis of in-situ electrical conductivity experiments, with
226 a cusp at 1700 $^{\circ}\text{C}$, 14 GPa, interpreted to correspond to the intersection of the calcite V
227 - aragonite reaction with the solidus, although quenched experiments (of Li et al. 2017)
228 performed with falling Pt-sphere show aragonite as run product down to 5.8 GPa,
229 1690 $^{\circ}\text{C}$. The dP/dT slope of the solidus for CaCO_3 proposed by Li et al (2017) therefore
230 markedly differs from MgCO_3 and FeCO_3 (Kang et al., 2015) and from results of other
231 groups on CaCO_3 . Our results at 12 GPa yield a melting temperature between 1850 and

232 1950 °C, inconsistent with a backbend, but consistent with Spivak et al. (2012).
233 Combined with the data to 6 GPa, our 12 GPa bracket leads to a high-pressure dP/dT
234 slope of the solidus similar to other carbonates.

235 We observed melting of magnesite at 6 GPa 1750 °C (Fig 1b), and between 1900
236 and 1950 °C at 12 GPa. Within experimental uncertainty all results on the melting curve
237 of magnesite are consistent except of a barely significant slightly higher melting
238 temperature in one experiment at 8 GPa by Katsura and Ito (1990), the bracket of
239 Shatskiy et al. (2018) locating ca. 50 °C lower and the experiments of Solopova et al.
240 (2015) also finding ca. 100 °C lower melting temperatures.

241 Run products in the binary mixture at 3 GPa, 1500 °C (Fig. 4), $X_{Ca} = 0.1$ and 0.2
242 display textures indicating fully molten charges without indications of a free fluid phase,
243 e.g. bubbles, contrary to the textures obtained by Shatskiy et al (2018) at these
244 conditions. At 1300 °C the liquid field remains wide, as shown by run CCMS10b, fully
245 molten at $X_{Ca} = 0.3$. This again differs from Shatskiy et al. (2018) where the liquid field
246 at 1300 °C, 3 GPa extends only from $X_{Ca} = 0.48$ to 0.63, as well as from Irving and
247 Wyllie (1975), which locate at 2.7 GPa (pressure corrected after Byrnes and Wyllie
248 1981) the liquidus minimum close to 1300 °C (see Fig. 2 for phase boundaries drawn
249 in each study). At 1250 °C complete melting is observed in mixtures at $X_{Ca} = 0.6$ and
250 0.7, the location of the liquidus constrained by the average analyses of dendrites at X_{Ca}
251 = 0.8 coexisting with Mg-calcite and at $X_{Ca} = 0.59$ coexisting with magnesite. Neither
252 charges run at 1225 °C or 1200 °C were fully molten. Microprobe analyses suggest that

253 the liquid field at 1225 °C extends from $X_{Ca} = 0.6$ to 0.7. At 1200 °C the estimated
254 compositions are irregularly distributed, altogether compatible with a minimum of the
255 liquidus surface at $X_{Ca} \approx 0.7$. Polygonal grain boundaries in run products at 1150 °C
256 and 1175 °C clearly indicate subsolidus conditions, the solvus between dolomite_{s.s.} and
257 magnesite_{s.s.} is intersected at bulk $X_{Ca} = 0.4$, 1200 °C, consistent with Irving and Wyllie
258 (1975).

259 A single experiment, CCMS9b at 1200 °C displays the occurrence of dolomite_{s.s.} +
260 liquid, providing information on the location of the peritectic reaction dolomite_{s.s.} =
261 liquid + magnesite_{s.s.}. Nevertheless, our data do not support a dolomite_{s.s.} + liquid field
262 extended over a temperature range of 100 °C as described by Irving and Wyllie (1975).
263 A narrow dolomite_{s.s.} + liquid field was also found in Shatskiy et al. (2018).

264 The data at 3 GPa as a whole suggest a pronounced asymmetry of melting of Ca-
265 Mg carbonates, as already observed by Irving and Wyllie (1975) at 2.7 GPa and by
266 Byrnes and Wyllie (1981) at 1.0 GPa. The two-phase liquid - magnesite loop remains
267 relatively tight, with a wide one phase liquid field, a shape also reported in Irving and
268 Wyllie (1975) and in Müller et al. (2017) at 6 GPa.

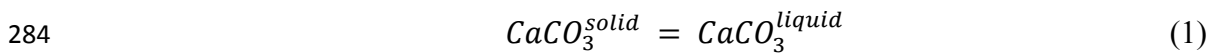
269 At 4.5 GPa (Fig. 4), completely molten experiments were observed at 1300 °C, at
270 bulk compositions $X_{Ca} = 0.6$ and 0.7, and at 1275 °C at $X_{Ca} = 0.6$. The assemblage Mg-
271 calcite + liquid was recovered for bulk composition $X_{Ca} = 0.3$ at 1275 °C. Sub-solidus
272 Mg-calcite/dolomite was present at 1250 °C for bulk composition $X_{Ca} = 0.6$ and 0.75.
273 The minimum of the liquidus at 4.5 GPa should be therefore located at $X_{Ca} \approx 0.60$ -0.65.

274

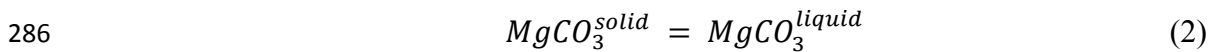
275 4. THERMODYNAMIC MODELLING

276 4.1. End member properties

277 Thermodynamic data on the pure carbonates constitute the basis for a ternary
278 (Ca,Mg,Fe²⁺)-carbonate melt solution model, which is a cornerstone for predicting
279 natural carbonate melting, carbonatite segregation, and metasomatic processes in the
280 mantle. While properties have been already derived for FeCO₃^{liquid} (Kang et al., 2015),
281 MgCO₃^{liquid} (Kang et al., 2016), CaCO₃^{liquid} (Zhao et al., 2019), a binary melt model for
282 CaCO₃ - MgCO₃ over a large range of pressure range is still lacking. In all likelihood,
283 the two endmember carbonates melt congruently at high pressures



285 and



287 as the quenched material on endmember compositions consisted entirely of calcite or
288 magnesite, and neither oxides or gas bubbles were detected. Elemental carbon, when
289 present, was found to occur in negligible amounts at capsule walls (note that siderite
290 melting is plagued by oxide and graphite formation, Tao et al. 2013, Kang et al. 2015).

291 For CaCO₃, our model is intended to reproduce phase relationships at mantle
292 temperatures and pressures where either aragonite or calcite V may be stable. The
293 complexities of the transformation from calcite I to calcite IV, and ultimately to calcite

294 V above ≈ 1000 °C (Ishizawa et al., 2013) are not considered here. Following the same
 295 procedure as described in Zhao et al. (2019) we re-fitted thermodynamic properties
 296 profiting from the new experimental data available. The standard molar Gibbs free
 297 energies G_0 (J), entropies S_0 (J/K), and selected volumetric properties were retrieved
 298 first by fitting the energy residue at conditions of the calcite V (ccV) - aragonite (ara)
 299 reaction, where $G_{ccV} = G_{ara}$, and then along the CaCO_3 melting curve, where $G_{ccV} =$
 300 $G_{\text{CaCO}_3}^{\text{liquid}}$ and $G_{ara} = G_{\text{CaCO}_3}^{\text{liquid}}$. Gibbs free energies of calcite V, and of $\text{CaCO}_3^{\text{liquid}}$, at
 301 the P-T conditions of the calcite V-aragonite transition, and of the CaCO_3 melting
 302 reaction were calculated from:

$$303 \quad G(P, T) = G(P_r, T_r) - \int_{P_r, T_r}^{P, T} S(P_r, T) dT + \int_{P_r, T_r}^{P, T} V(P, T) dP \quad (3)$$

$$304 \quad = G(P_r, T_r) + \int_{P_r, T_r}^{P, T} C_p(P_r, T) dT - T * \int_{P_r, T_r}^{P, T} \left[\frac{C_p(P_r, T)}{T} \right] dT + \int_{P_r, T_r}^{P, T} V(P, T) dP$$

305 The isobaric heat capacity function $C_p(T)$ adopted is:

$$306 \quad C_p = c_1 + c_2 \times T + \frac{c_3}{T^2} + \frac{c_5}{\sqrt{T}} \quad (4)$$

307 Coefficients for the heat capacity functions for aragonite and calcite V were modified
 308 to converge to the Dulong-Petit limit at high temperature (> 2000 K) as:

$$309 \quad C_p = 3 \times R \times n + \alpha_T^2 \times V_T \times K_T \times T \quad (5)$$

310 where R is the gas constant, n the number of atoms in the substance of interest, and α_T
 311 the temperature dependent thermal expansion coefficient:

$$312 \quad \alpha_T = \alpha_0 \times \left(1 - \frac{10}{\sqrt{T}} \right). \quad (6)$$

313 Volume at 1 bar, reference pressure $V(T, P_r)$ is

314
$$V(T, P_r) = V_0 \times [1 + \int_{T-T_r}^T \alpha(T, P_r) dT], \quad (7)$$

315 and the temperature dependent bulk modulus K_T is given by:

316
$$K_T = K_0 \times [1 - B \times (T - 298.15)] \quad (8)$$

317 where $B = 1.5 \times 10^{-4}$ is used for solids, after Holland and Powell (1998).

318 At low temperatures (< 500 K), the C_p functions were fitted consistent with the heat
319 capacities from Holland and Powell (2011).

320 The specific heat for liquids was constrained to follow the Dulong Petit criterion (eq.
321 5) similarly to solids (Iwashita et al, 2013). A term $c_4 \times T^2$ was then required in the
322 C_p function (eq. 4) of the $MgCO_3^{liquid}$.

323 Volumes at elevated pressures are computed by the Murnaghan equation of state:

324
$$V(T, P) = V(T, P_r) \times \left[1 - K' \times \frac{P}{(K' \times P + K(T, P_r))} \right]^{\frac{1}{K'}} \quad (9)$$

325 The thermodynamic analysis was performed by adopting G_0 and S_0 of aragonite
326 from Königsberber et al. (1999) and values of V_0 , α_0 , K_0 and K' for aragonite and calcite
327 V are from Zhao et al. (2019). The properties of $MgCO_3^{liquid}$ and $CaCO_3^{liquid}$ were
328 fitted constraining volumes to approach the compression curves (Fig. 5) modelled in
329 Hurt and Wolf (2020), using the average thermal expansion coefficient of $0.164 \cdot 10^{-3}$
330 K^{-1} (at 1100 K) of Hurt and Lange (2019) for alkaline earth carbonate liquids. Our best
331 fit was found to closely approach expected molar volume for $CaCO_3^{liquid}$, whereas
332 molar volumes for $MgCO_3^{liquid}$ lie mid-way between the expected compression curve

333 of $MgCO_3^{liquid}$ for 6-fold Mg-C coordination and the model obtained by molecular
334 dynamics (Hurt and Wolf, 2020), where Mg-C coordination changes from 4-fold at low
335 to 6-fold at high pressure.

336 The results of the non-linear least-square fit are presented in Table 2, and the phase
337 diagrams for the system CaO-CO₂ and MgO-CO₂ computed employing Perplex
338 (Connolly 2009) and data from Holland and Powell (2011) are reported in Fig. 1, along
339 with available experimental data. As previously noted, experimental data and
340 thermodynamic analysis suggest only moderate differences in the behaviour of
341 $CaCO_3^{liquid}$ and $MgCO_3^{liquid}$, in particular in the dP/dT slopes of the melting reactions,
342 yet, decarbonation instead of melting occurs with calcite to 4 MPa (1240 °C, Baker,
343 1962) while magnesite decomposes to periclase+CO₂ to 2.5 GPa (1520 °C, Irving and
344 Wyllie, 1975).

345

346 **4.2. Solution models for CaCO₃-MgCO₃ liquid**

347 Despite the importance of the CaCO₃-MgCO₃ binary, a model for carbonate liquids
348 in this system does not exist, possibly because of the complexities in experimental data
349 previously discussed. Here we present a first thermodynamic analysis showing a large
350 non-ideality of the carbonate liquid. Fitting of the thermodynamic properties for the
351 liquid was performed compromising between the experimental data at 1.0 GPa of
352 Byrnes and Wyllie (1981), our results at 3.0 GPa and 4.5 GPa, and data at 6 GPa from
353 Muller et al. (2017). The criterion for such a selection is that the location of the minima

354 in Byrnes and Wyllie (1981) and Müller et al. (2017) remain approximately in the range
 355 of our study with a moderate decrease of X_{Ca} from ≈ 0.68 at 1 GPa, to 0.60-0.65 at 3
 356 and 6 GPa. This is consistent with the observation of the composition of carbonatitic
 357 liquids with $X_{Ca} = 0.60-0.63$ in the model systems CMAS at 2.4-3.0 GPa (Dalton and
 358 Presnall, 1998; Novella et al., 2014) and a moderate decrease in the minimum's X_{Ca}
 359 with pressure. On the contrary, in Shatskiy et al. (2018), a shift to higher X_{Ca} values has
 360 been proposed, from $X_{Ca} \approx 0.53$ at 3 GPa to $X_{Ca} \approx 0.62$ at 6 GPa. The position of the
 361 minimum in Buob et al. (2006), 6 GPa, is little constrained, the experiments allow a
 362 minimum between $X_{Ca} \approx 0.45$ and 0.65.

363 To derive a thermodynamic model for carbonate melts that describes the
 364 asymmetry discussed above, we used the van Laar model for solids by Franzolin et al.
 365 (2011, page 222) and a subregular mixing model (see formulation in Will 1998, page
 366 69) for the liquid, with Margules parameters w_{ij} pressure and/or temperature
 367 dependent according to the expression:

$$368 \quad w_G = w_H + w_s T + w_V P \quad (10)$$

369 Since carbonate liquids are molten salts, we first assumed that a binary mixture
 370 between $CaCO_3^{liquid}$ and $MgCO_3^{liquid}$ with two liquid endmembers should be able to
 371 properly describe the phase relations. The unknown interaction parameter
 372 $w_{CaCO_3-MgCO_3}^{liquid}$ and $w_{MgCO_3-CaCO_3}^{liquid}$ were retrieved by minimizing residues of the
 373 equalities:

$$374 \quad \mu_{CaCO_3}^*^{liquid} + RT \ln X_{CaCO_3}^{Ca-liquid} + RT \ln \gamma_{CaCO_3}^{Ca-liquid} = \mu_{calcite}^* + RT \ln X_{CaCO_3}^{calcite} + RT \ln \gamma_{CaCO_3}^{calcite} \quad (11)$$

$$375 \quad \mu_{MgCO_3}^*_{liquid} + RT \ln X_{MgCO_3}^{Ca-liquid} + RT \ln \gamma_{MgCO_3}^{Ca-liquid} = \mu_{magnesite}^* + RT \ln X_{MgCO_3}^{calcite} + RT \ln \gamma_{MgCO_3}^{calcite} \quad (12)$$

$$376 \quad \mu_{CaCO_3}^*_{liquid} + RT \ln X_{CaCO_3}^{Mg-liquid} + RT \ln \gamma_{CaCO_3}^{Mg-liquid} = \mu_{calcite}^* + RT \ln X_{CaCO_3}^{magnesite} +$$

$$377 \quad RT \ln \gamma_{CaCO_3}^{magnesite} \quad (13)$$

$$378 \quad \mu_{MgCO_3}^*_{liquid} + RT \ln X_{MgCO_3}^{Mg-liquid} + RT \ln \gamma_{MgCO_3}^{Mg-liquid} = \mu_{magnesite}^* + RT \ln X_{MgCO_3}^{magnesite} +$$

$$379 \quad RT \ln \gamma_{MgCO_3}^{magnesite} \quad (14)$$

380 where μ_i^* (Chatterjee, 1991) is the standard chemical potential of i at pressure and
 381 temperature of interest (i.e. the experimental conditions), *Ca-liquid* stands for the liquid
 382 in equilibrium with calcite solid solution, and *Mg-liquid* the liquid with magnesite s.s.
 383 μ_i^* are calculated profiting of the data extracted on melting of calcite/aragonite and
 384 magnesite. Results are presented in Table 3, and Fig. 6 shows the phase diagram at 3
 385 and 6 GPa calculated using Perplex (Connolly 2005).

386 The two-endmember model yields large interaction parameters w_H , up to ≈ -100 kJ,
 387 to force asymmetry on the Ca-side. In the binary $FeCO_3$ - $MgCO_3$ (Kang et al. 2016), the
 388 large temperature difference of melting temperatures for siderite and magnesite controls
 389 asymmetry of the minimum close to the iron component, and low interaction parameters
 390 are required ($w_H = -7.6$ kJ). Differently, calcite/aragonite and magnesite melt at very
 391 similar temperatures, asymmetry is hence only obtained with a large non-ideality.
 392 Furthermore, a value for w_V is necessary as the relative positions of calcite and
 393 magnesite melting intersect at 3.8 GPa (Fig. 1). The calculated phase diagrams (Fig. 6)
 394 are characterized by large solid-liquid loops, which fail to reproduce the experimental
 395 constraints used here, as well as the liquid field found in Shtaskiy et al. (2018) at 3 GPa.
 396 The stability of liquids with a much wider compositional range around the dolomitic

397 composition therefore implies the need of using an intermediate component. Although
 398 unexpected from the principally ionic structure of carbonate melts, this $\text{Ca}_{0.5}\text{Mg}_{0.5}\text{CO}_3$ -
 399 component permits the tuning of the liquidus surface and the composition of the
 400 peritectic liquid.

401 In a second step we therefore add the component $\text{Ca}_{0.5}\text{Mg}_{0.5}\text{CO}_3^{liquid}$, which
 402 thermodynamic properties are defined as a linear combination of CaCO_3^{liquid} and
 403 MgCO_3^{liquid} . As a consequence, two additional equalities apply:

$$404 \quad \mu_{\text{Mg}_{0.5}\text{Ca}_{0.5}\text{CO}_3}^* + RT \ln X_{\text{Mg}_{0.5}\text{Ca}_{0.5}\text{CO}_3}^{Ca-liquid} + RT \ln \gamma_{\text{Mg}_{0.5}\text{Ca}_{0.5}\text{CO}_3}^{Ca-liquid} =$$

$$405 \quad \mu_{\text{dolomite}}^* + RT \ln X_{\text{Mg}_{0.5}\text{Ca}_{0.5}\text{CO}_3}^{\text{calcite}} + RT \ln \gamma_{\text{Mg}_{0.5}\text{Ca}_{0.5}\text{CO}_3}^{\text{calcite}} \quad (15)$$

$$406$$

$$407 \quad \mu_{\text{Mg}_{0.5}\text{Ca}_{0.5}\text{CO}_3}^* + RT \ln X_{\text{Mg}_{0.5}\text{Ca}_{0.5}\text{CO}_3}^{Mg-liquid} + RT \ln \gamma_{\text{Mg}_{0.5}\text{Ca}_{0.5}\text{CO}_3}^{Mg-liquid} =$$

$$408 \quad \mu_{\text{dolomite}}^* + RT \ln X_{\text{Mg}_{0.5}\text{Ca}_{0.5}\text{CO}_3}^{\text{magnesite}} + RT \ln \gamma_{\text{Mg}_{0.5}\text{Ca}_{0.5}\text{CO}_3}^{\text{magnesite}} \quad (16)$$

409 For sake of simplicity, we neglect the equalities which relate $\mu_{\text{CaCO}_3}^{Mg-liquid}$, $\mu_{\text{MgCO}_3}^{Mg-liquid}$,
 410 and $\mu_{\text{Mg}_{0.5}\text{Ca}_{0.5}\text{CO}_3}^{liquid}$ with disordered dolomite (i.e. equilibria below the peritectic point)
 411 because of the scarce experimental data available. $X_{\text{Mg}_{0.5}\text{Ca}_{0.5}\text{CO}_3}^{Mg-liquid}$ are optimized on the
 412 fitting procedure. Tuning of the w_{ij} parameters was at last performed on a trial-and-
 413 error basis, given their strong interdependence. The Δw_G ($w_{\text{CaCO}_3-\text{MgCO}_3} -$
 414 $w_{\text{MgCO}_3-\text{CaCO}_3}$) is again unexpectedly very large, in the order of 100 kJ at the P-T range
 415 of interest. Lower values do not account for the depression of the solidus in the order
 416 of 400 °C, and especially for the asymmetry of the minimum.

417 As shown in Fig. 7, the model is able to reproduce exactly the position of the

418 minimum at 1 GPa, 3 GPa, 4.5 GPa, and 6 GPa in the aforementioned studies. At 1 GPa
419 (Fig. 7) the model closely matches the liquidus surface; however, on the Mg rich side,
420 the reaction magnesite = periclase + CO₂ is predicted at a temperature higher than the
421 minimum, leading to a field magnesite + liquid not observed in Byrnes and Wyllie
422 (1981). As this field results from the thermodynamic properties of the solid or gas
423 phases, it is not further treated here. At 3 GPa the model does not fit one experiment at
424 1300 °C, which result is entirely molten at $X_{Ca} = 0.3$ and would require a very "flat"
425 shape of the liquidus. Interaction parameters (w_H and w_V for interactions
426 Ca_{0.5}Mg_{0.5}CO₃-MgCO₃) were tuned to fit the magnesite-liquid loop similar to what was
427 observed by Irving and Wyllie (1975). The phase diagram at 6 GPa was calculated
428 omitting aragonite, to allow direct comparison with the results by Müller et al. (2017).
429 The model closely approaches experimental data for the liquid–magnesite loop,
430 whereas it predicts a larger field for calcite V - liquid. However, aragonite is expected
431 to modify the topology above 4.5 GPa (Fig. 7), according to Zhao et al. (2019) the field
432 liquid + dolomite is restricted close to the minimum of the binary, to temperatures <
433 1280 °C and $0.4 < X_{Ca} < 0.8$, whereas aragonite is on the liquidus from 1280 °C to
434 1560 °C, the temperatures of the aragonite - calcite V transformation. This topology
435 has not been experimentally reproduced yet, but is an intrinsic feature of the phase
436 diagram, although the absolute values of $P/T/X_{Ca}$ depend on the location of the disputed
437 aragonite - calcite transformation (Li et al., 2017; Zhao et al., 2019; Litasov et al., 2020).
438 When aragonite is included in calculations, at 6 GPa the stability field of dolomite is
439 restricted to $0.4 < X_{Ca} < 0.45$ (Fig. 7, orange curves). The width of this field (compare

440 Fig. 7 at 4.5 and 6 GPa) is controlled by the properties of the thermodynamic model
441 predicting disordered carbonate (Franzolin et al., 2011) compared to aragonite (this
442 work), and relates to the reaction boundary aragonite + magnesite = dolomite (Fig. S1),
443 experimentally investigated by Luth (2001), Buob et al. (2006), Hermann et al. (2016)
444 among others, not reproduced in the model presented here.

445 A simple direct application of the melt model is the melting diagram for a dolomite
446 composition (Fig. S1). The minimum pressure of direct dolomite melting is 0.77 GPa
447 (1080 °C), which compares to 0.004 and 2.5 GPa for calcite and magnesite, respectively.
448 As expected, melting is incongruent (e.g. Persikov and Bukhtiyarov, 2004) and liquids
449 on dolomite stoichiometry only become stable at ~2 GPa, 1500 °C, which has direct
450 bearings on the more complex Si- and Al-bearing simple systems approximating mantle
451 compositions.

452

453 **5. THE MELTING OF CARBONATED MANTLE**

454 The model for carbonate liquids can be successfully applied to evaluate the
455 consistency of experimental studies on the melting of carbonated peridotites, and to
456 extrapolate experimental results to the pressure-temperature range where primary Si-
457 and Al-poor carbonatitic liquids could form. The systems CMS·CO₂ and CMAS·CO₂
458 constitute simple model systems allowing for carbonatite and silica undersaturated
459 melts analogue to a lherzolithic mantle (Wyllie and Huang 1976; Egglar 1976). The
460 solidus of a carbonated lherzolithic mantle in CMS·CO₂ is defined by the coexistence of

461 the five-phase assemblage olivine, orthopyroxene, clinopyroxene, dolomite or
462 magnesite and liquid, which is extended to six phases by garnet in the 5-component
463 CMAS·CO₂ system. The solidus is univariant in P-T space, and characterized by two
464 invariant points: the first is generated by the intersection of the solidus with the reaction
465 dolomite + 4 enstatite = diopside + 2 forsterite + 2 CO₂ leading to the so called "solidus
466 ledge" at 2.3-2.8 GPa (Novella et al., 2014 and references therein), its pressure location
467 and extent being related to the abundance of silicate component in the liquid; the second
468 invariant point is located at higher pressures, where magnesite forms through the
469 reaction 2 enstatite + dolomite = diopside + 2 magnesite (Brey et al., 1983). As both
470 carbonate and clinopyroxene are solid solutions in CMS, their compositions vary on
471 the univariant line and the appearance of magnesite does not necessarily imply the
472 consumption of dolomite. At high bulk Ca/Mg ratio and excess CO₂, dolomite persists
473 at the expense of orthopyroxene.

474

475 **5.1 Melting phase relations**

476 The studies of Eggler (1976), and Canil and Scarfe (1990) experimentally
477 constrained the solidus of model peridotites in CMS·CO₂ at \approx 1250 °C, 3 GPa, and \approx
478 1370 °C, 9 GPa. In both studies the liquid was reconstructed to be broadly kimberlitic
479 in composition. Experiments in CMAS·CO₂ by Canil and Scarfe (1990) combined with
480 results at 2.8 GPa from Adam (1988) suggest a lower dP/dT slope for the solidus in the
481 Al-bearing system, and a lowering by \approx 50-70 °C of the solidus in CMAS·CO₂

482 compared to CMS·CO₂ (at 4 GPa). Dalton and Presnall (1998a, 1998b) performed an
483 experimental survey of liquid compositions in CMAS·CO₂ and found carbonatitic
484 liquids on the solidus, rapidly evolving to melilitic to kimberlitic compositions with
485 increasing temperature and pressure (Gudfinnsson and Presnall, 2005). Presnall and
486 coworkers found the dP/dT slope of the solidus in CMAS·CO₂ to be similar to Canil
487 and Scarfe (1990), but located more than 100 °C higher at 7 GPa. Similarly, the
488 temperature difference of the solidus in CMS·CO₂ is ≈ 200 °C between Canil and Scarfe
489 (1990) and the Presnall-group. These discrepancies are discussed in Dalton and Presnall
490 (1998a, their figure 5 for comparison), who suggested that the solidi in CMS·CO₂ and
491 CMAS·CO₂ should have very similar dP/dT -slopes as the Al-solubility in the
492 carbonatitic melt is low, hence garnet has a very minor contribution to the melting
493 reaction. In this frame, Presnall and coworkers proposed that the CMS-CO₂ solidus
494 should be located ≈ 50 °C higher than in CMAS-CO₂ and not lower as indicated by the
495 results of Canil and Scarfe (1990), and ascribed differences to accuracy in temperature
496 measurement in the experiments by Canil and Scarfe (1990). This suggestion would be
497 adequate if, for a given pressure, the solidus melt would always be on the minimum and
498 buffered by the same phase assemblage, below we show that this is not the case.

499 These discrepancies can now be modelled in pseudosections calculated on the bulk
500 compositions of Canil and Scarfe (1990), Dalton and Presnall (1998a) and Gudfinnsson
501 and Presnall (2005). These calculations are performed using the solution models for
502 olivine, pyroxenes and garnet from Jennings and Holland (2015), carbonates from
503 Franzolin et al. (2011), and the liquid model presented here. A sensitivity analysis was

504 performed varying solution models for orthopyroxene, clinopyroxene and garnet.

505 Fig. 8a shows the excellent match of the modelled phase relationships for the system
506 CMS·CO₂ with experimental results in Canil and Scarfe (1990), which do not constitute
507 an input into the melt model. The subsolidus assemblage above 4 GPa is composed of
508 olivine, clinopyroxene and carbonate. The solidus at 7 GPa is predicted to be at 1340 °C,
509 i.e. within the 1300-1350 °C experimental bracket, and a wedge shaped, divariant field,
510 olivine + clinopyroxene + magnesite + carbonate liquid forms at higher temperature,
511 consistent with the available experiments.

512 Nevertheless, the calculated position of the reaction



514 expands the subsolidus stability field of magnesite by 100 °C compared to the
515 experimental determination by Brey et al. (1983). The P-T-position of this reaction is
516 strongly affected by the Ca-Mg partitioning between clinopyroxene and carbonate solid
517 solutions, which is not an object of this study. More important, the appearance of
518 magnesite does not necessarily imply complete dolomite consumption, for bulk
519 composition CCMS2 of Canil and Scarfe (1990), we predict a 1.2 GPa wide field of
520 coexisting dolomite and magnesite on the solidus (2.8 to 4 GPa).

521 Calculation of the pseudosection for the bulk used by Dalton and Presnall (1998a) in
522 CMAS·CO₂ (Figure 8b) reveal a shift of the solidus to higher temperatures than in
523 CMS-CO₂, in excellent agreement with experimental data, only the low-pressure
524 experimental brackets on the solidus are not exactly matched. The solidus at 7.5 GPa is

525 located at ≈ 1420 °C, 70 °C higher than in the Al_2O_3 -free bulk composition used in Canil
526 and Scarfe (1990), but 50 °C lower than the solidus in $\text{CMS}\cdot\text{CO}_2$ determined by Dalton
527 and Presnall (1998a, their Figure 5). These observations are not necessarily inconsistent
528 as the bulk composition of the experiments in $\text{CMS}\cdot\text{CO}_2$ reported by Dalton and
529 Presnall (1998a) is not available. The “ledge” of the solidus is predicted at a pressure
530 of 2 GPa, at least 0.5 GPa lower than experimentally determined for $\text{CMAS}\cdot\text{CO}_2$
531 (Novella et al., 2014, and references therein). This is likely a result of the silicate
532 component in the melt close to the ledge and/or of the expansion of the solid carbonate
533 field compared to CO_2 vapor (i.e. the EoS used for CO_2) + clinopyroxene. Furthermore,
534 it has to be stressed that the occurrence of a ledge is not an omnipresent or intrinsic
535 feature of phase relations in carbonated ultramafics, but relates to the stable subsolidus
536 assemblage, i.e., to the bulk composition assumed.

537 As already discussed in Egglar (1976, his Fig. 3b) the ledge is not predicted for
538 compositions undersaturated in orthopyroxene, which is consistently confirmed by our
539 calculations presented in Fig. 8a. Similarly, as an example of a bulk enriched in
540 (metasomatic) dolomitic carbonate, we explore the phase relations in bulk composition
541 JASCM-3 (Fig. 8c) from Gudfinnsson and Presnall (2005). Here, the solidus is located
542 at remarkably lower temperature compared to the bulk composition used in Dalton and
543 Presnall (1998a), and lower than Canil and Scarfe (1990). Furthermore, on the solidus
544 and in the subsolidus, dolomite and magnesite coexist over a very large pressure range.
545 The lherzolite assemblage is therefore not stable on the solidus, and the ledge is
546 remarkably absent. These observations highlight the importance of heterogeneities in

547 composition of a carbonated mantle, where the carbonate is necessarily added by
548 metasomatic processes, and in particular of the orthopyroxene/carbonate proportion
549 (highly affected by such processes), in controlling the appearance of carbonatitic liquids.

550

551 **5.2. Melt compositions**

552 The (grossly dolomitic) composition of the carbonatitic liquid on the solidus of
553 carbonated peridotites has often been interpreted as representing the location of the
554 minimum in the system $\text{CaCO}_3\text{-MgCO}_3$ (Dalton and Presnall 1998a, pag. 132; Figure
555 4 in Buob et al. 2006). This interpretation automatically implies that bulk composition
556 (e.g. Ca/Mg ratio and Al_2O_3) could not alter significantly phase relationships in a low
557 variance assemblage. However, as shown in Fig. 7, experimental data at high pressure
558 support a large stability field for liquid, and a large variation of $X_{\text{Ca}}^{\text{liquid}}$ as a function of
559 temperature and pressure when coexisting with dolomite or magnesite. Notably the
560 pressure dependence of the "saddle" on the liquidus at 1400-1500 °C, $X_{\text{Ca}} \approx 0.5$ strongly
561 influences variations in liquid composition.

562 In the calculated CMS- CO_2 -phase diagram of Fig. 8a, melt compositions do not remain
563 in the minimum, hence melting temperatures are bulk composition dependent. The X_{Ca}
564 of the liquid on the solidus shifts with pressure, and calculated melt composition
565 isopleths reverse their dP/dT slope with temperature: across the carbonate liquid +
566 clinopyroxene + magnesite + olivine wedge (i.e. between the red solidus curve and the
567 blue carbonate-out curve in Fig. 8a), the X_{Ca} in the liquid decreases until magnesite is

568 exhausted, then remains constant with clinopyroxene + orthopyroxene + olivine, and
569 then gently increases with increasing temperature above the stability of orthopyroxene.
570 That melting exhausts orthopyroxene is predicted above ≈ 1450 °C, only ≈ 50 °C higher
571 than the experimental observation. This small discrepancy is likely attributable to an
572 increase of SiO₂ in the melt, a melt-component not modelled here.

573 In the calculated CMAS-CO₂-phase diagram (Fig. 8b), the X_{Ca} of the liquid on the
574 calculated solidus shifts from ≈ 0.65 at ≈ 3 GPa to ≈ 0.45 at 7-8 GPa, as found by Dalton
575 and Presnall (1998b). At high pressure, this value is significantly higher than the
576 composition of the minimum in the simple binary system (Fig. 7), consistent with a
577 solidus temperature ≈ 80 °C higher than the minimum temperature in the binary.

578 As an overall conclusion resulting from the experimental data and modelled phase
579 relations, the solidii are generally not in the carbonate-melt minimum and hence their
580 temperature and melt composition bulk composition dependent. The first-glance
581 contradiction between the Presnall-group experiments in CMAS·CO₂ and Canil and
582 Scarfe (1990) in CMS-CO₂ is hence only apparent, both datasets are consistent with
583 calculated phase relations.

584 Finally, a word of caution: The experimental investigations and thermodynamic
585 modelling in CM(A)S-CO₂ yield phase relations in a system that models a lherzolitic
586 mantle but not necessarily the genesis and composition of natural carbonatites. For
587 these latter, additional components, notably H₂O and alkali depress the solidus of
588 carbonated lithologies by >500 °C and strongly modify melt compositions as both H₂O

589 and alkali partition into the carbonatite melt (e.g. Dasgupta and Hirschmann 2007b,
590 Weidendorfer et al., 2017, 2020; Pintér et al., 2021; Shatskiy et al. 2022). In particular
591 the onset of melting in a carbonated mantle is governed by such minor components.
592 Trivially enough, melting of a carbonated mantle requires carbonate, which is a
593 question of redox state and temperature. The asthenospheric mantle is too hot for
594 carbonate stability (Dasgupta and Hirschmann, 2010; Rohrbach and Schmidt, 2011),
595 the deeper mantle too reduced for carbonates, and the lithospheric mantle should only
596 contain carbonate where metasomatized. It is not the purpose of this contribution to
597 speculate on carbonatite origin, but to provide a first step towards enabling
598 thermodynamic models of carbonate melting.

599

600 **6. CONCLUSIONS**

601 Although CaCO_3 and MgCO_3 melt at similar temperatures over a very large pressure
602 range, the liquidus surface in the binary system is markedly asymmetric, the minimum
603 located at $X_{\text{Ca}} \approx 0.65$ and at temperatures ≈ 400 °C below the melting of
604 calcite/aragonite or magnesite. The liquidus at $X_{\text{Ca}} \approx 0.30$ - 0.50 on the liquid-magnesite
605 loop shows a characteristic "saddle", whose thermodynamic modelling heavily
606 influences the compositional evolution of partial carbonate liquids. Unexpectedly, such
607 features require a three-component melt solution model, with large non-ideal
608 interaction parameters for $\text{Ca}_{0.5}\text{Mg}_{0.5}\text{CO}_3$.

609 Calculated pseudosections demonstrate the sensitivity of the location of the solidus

610 on the relative abundances of carbonate and orthopyroxene, as determined by the bulk
611 composition selected. The width of low-variance field olivine + clinopyroxene +
612 orthopyroxene + carbonate liquid in the model system CaO-MgO-SiO₂-CO₂ (+ garnet
613 with Al₂O₃) varies by 100 °C as a function of the MgO/CaO ratio and CO₂ availability.

614

615 **ACKNOWLEDGMENTS**

616 This work has been supported by the NSF of China (Grant No. 41204060), Open Fund
617 from Hubei Subsurface Multi-scale Imaging Key Laboratory (China University of
618 Geosciences), and Scholarship from support to S.Z. as Visiting Scholar from China Scholarship
619 Council during her stay at Milan University is greatly appreciated. S.T and S.P. acknowledge
620 support from MIUR-PRIN, grant 2017ZE49E7_002. We thank Rajdeep Dasgupta for editorial
621 handling and two anonymous reviewers who provided thoughtful feedback that improved the
622 study.

623

624 **APPENDIX A. SUPPLEMENTARY MATERIAL**

625 Supplementary material to this article can be found online

626 Research data include thermodynamic entries for Perplex software package (Connolly,
627 2009).

628

629

630 **REFERENCES**

631 Adam J. (1988) Dry, Hydrous, and CO₂-Bearing Liquidus Phase Relationships in the
632 Cmas System at 28 Kb, and Their Bearing on the Origin of Alkali Basalts. *J. Geol.*
633 **96**, 709-719.

634 Baker E. H. (1962) The calcium oxide–carbon dioxide system in the pressure range 1—
635 300 atmospheres. *J. Chem. Soc.* **87**, 464-470.

636 Brey G., Brice W.R., Ellis D.J., Green D.H., Harris K.L. and Ryabchikov I.D., (1983)
637 Pyroxene-carbonate reactions in the upper mantle. *Earth Planet. Sci. Lett.* **62**, 63-74.

638 Buob A., Luth R. W., Schmidt M. W. and Ulmer P. (2006) Experiments on CaCO₃-
639 MgCO₃ solid solutions at high pressure and temperature. *Am. Mineral.* **91**, 435-440.

640 Byrnes A. P. and Wyllie P. J. (1981) Subsolidus and melting relations for the join
641 CaCO₃-MgCO₃ at 10 kbar. *Geochim. Cosmochim. Acta* **45**, 321-328.

642 Canil D. and Scarfe C. M. (1990) Phase relations in peridotite+ CO₂ systems to 12 GPa:
643 implications for the origin of kimberlite and carbonate stability in the Earth's upper
644 mantle. *J. Geophys. Res. Solid Earth* **95**, 15805-15816.

645 Chakhmouradian A. R. and Zaitsev A. N. (2012). Rare earth mineralization in igneous
646 rocks: sources and processes. *Elements*, **8**, 347-353.

647 Chatterjee N. D. (2013). *Applied mineralogical thermodynamics: selected topics.*
648 Springer Science & Business Media.

649 Connolly J. A. D. (2005) Computation of phase equilibria by linear programming: A

650 tool for geodynamic modeling and its application to subduction zone decarbonation.
651 *Earth Planet. Sci. Lett.* **236**, 524-541.

652 Connolly J.A.D. (2009) The geodynamic equation of state: what and how. *Geochem.*
653 *Geophys. Geosys.* **10**, Q10014

654 Dalton J. A. and Presnall D. C. (1998a) Carbonatitic melts along the solidus of model
655 lherzolite in the system CaO-MgO-Al₂O₃-SiO₂-CO₂ from 3 to 7 GPa. *Contrib.*
656 *Mineral. Petrol.* **131**, 123-135.

657 Dalton J. A. and Presnall D. C. (1998b) The continuum of primary carbonatitic-
658 kimberlitic melt compositions in equilibrium with lherzolite: Data from the system
659 CaO-MgO-Al₂O₃-SiO₂-CO₂ at 6 GPa. *J. Petrol.* **39**, 1953 – 1964.

660 Dasgupta R. and Hirschmann M. M. (2006). Melting in the Earth's deep upper mantle
661 caused by carbon dioxide. *Nature* **440**, 659-662.

662 Dasgupta R., Hirschmann M. M. and Dellas N. (2005) The effect of bulk composition
663 on the solidus of carbonated eclogite from partial melting experiments at 3 GPa.
664 *Contrib. Mineral. Petrol.* **149**, 288-305.

665 Dasgupta R. and Hirschmann M. M. (2007a). A modified iterative sandwich method
666 for determination of near-solidus partial melt compositions. II. Application to
667 determination of near-solidus melt compositions of carbonated peridotite. *Contrib.*
668 *Mineral. Petrol.* **154**, 647-661

669 Dasgupta R. and Hirschmann M. M. (2007b) Effect of variable carbonate concentration

670 on the solidus of mantle peridotite. *Am. Mineral.* **92**, 370-379.

671 Dasgupta R. and Hirschmann M. M. (2010) The deep carbon cycle and melting in
672 Earth's interior. *Earth Planet. Sci. Lett.* **298**, 1-13.

673 Eggler D. H. (1976). Does CO₂ cause partial melting in the low-velocity layer of the
674 mantle? *Geology* **4**, 69-72.

675 Franzolin E., Schmidt M. W. and Poli S. (2011) Ternary Ca-Fe-Mg carbonates:
676 subsolidus phase relations at 3.5 GPa and a thermodynamic solid solution model
677 including order/disorder. *Contrib. Mineral. Petrol.* **161**, 213-227.

678 Gaillard F., Malki M., Iacono-Marziano G., Pichavant M and Scaillet B. (2008)
679 Carbonatite Melts and the electrical conductivity of the asthenosphere. *Science*, **322**,
680 1363-1365.

681 Grassi D. and Schmidt M. W. (2011) The melting of carbonated pelites from 70 to 700
682 km depth. *J. Petrol.* **52**, 765-789.

683 Gudfinnsson G. H. and Presnall D. C. (1996) Melting relations of model Iherzolite in
684 the system CaO-MgO-Al₂O₃-SiO₂ at 2.4-3.4 GPa and the generation of komatiites.
685 *J. Geophys. Res.* **101**, B12: 27701-27709.

686 Gudfinnsson G. H. and Presnall D. C. (2005) Continuous gradations among primary
687 carbonatitic, kimberlitic, melilititic, basaltic, picritic, and komatiitic melts in
688 equilibrium with garnet Iherzolite at 3-8GPa. *J. Petrol.* **46**, 1645-1659.

689 Hammouda T. (2003) High-pressure melting of carbonated eclogite and experimental

690 constraints on carbon recycling and storage in the mantle. *Earth Planet. Sci. Lett.*
691 **214**, 357-368.

692 Hammouda T. and Keshav S. (2015) Melting in the mantle in the presence of carbon:
693 Review of experiments and discussion on the origin of carbonatites. *Chem. Geol.* **418**,
694 171-188.

695 Hermann J., Troitzsc, U. and Scott D. (2016) Experimental subsolidus phase relations
696 in the system $\text{CaCO}_3\text{-CaMg}(\text{CO}_3)_2$ up to 6.5 GPa and implications for subducted
697 marbles. *Contrib. Mineral. Petrol.* **171**, 1-17.

698 Hofmann A.W., Farnetani C.G., Spiegelman M. and Class C. (2011) Displaced helium
699 and carbon in the Hawaiian plume. *Earth Planet. Sci. Lett.* **312**, 226-236.

700 Holland T. J. B. and Powell R. (1998) An internally consistent thermodynamic data set
701 for phases of petrological interest. *J. Metamorph. Geol.* **16**, 309-343.

702 Holland T. J. B. and Powell R. (2011) An improved and extended internally consistent
703 thermodynamic dataset for phases of petrological interest, involving a new equation
704 of state for solids. *J. Metamorph. Geol.* **29**, 333-383.

705 Hurt S. M. and Lange R. A. (2019) The density of $\text{Li}_2\text{CO}_3\text{-Na}_2\text{CO}_3\text{-K}_2\text{CO}_3\text{-Rb}_2\text{CO}_3\text{-}$
706 $\text{Cs}_2\text{CO}_3\text{-CaCO}_3\text{-SrCO}_3\text{-BaCO}_3$ liquids: New measurements, ideal mixing, and
707 systematic trends with composition. *Geochim. Cosmochim. Acta* **248**, 123-137.

708 Hurt S. M. and Wolf A. S. (2020) Anomalous structure of MgCO_3 liquid and the
709 buoyancy of carbonatite melts. *Earth Planet. Sci. Lett.* **531**, 115927.

- 710 Irving A. J. and Wyllie P. J. (1975) Subsolidus and melting relationships for calcite,
711 magnesite and the join $\text{CaCO}_3\text{-MgCO}_3$ 36 kb. *Geochim. Cosmochim. Acta* **39**, 35-
712 53.
- 713 Iwashita T., Nicholson D. M. and Egami T. (2013) Elementary excitations and
714 crossover phenomenon in liquids. *Phys. Rev. Lett.* **110**, 205504.
- 715 Jennings E. S. and Holland T. J. B. (2015) A simple thermodynamic model for melting
716 of peridotite in the system NCFMASOcr. *J. Petrol.* **56**, 869-892.
- 717 Jones A. P., Genge M. and Carmody L. (2013) Carbonate melts and carbonatites. *Rev.*
718 *Mineral. Geochem.* **75**, 289-322.
- 719 Kang N., Schmidt M. W., Poli S., Connolly J. A. D. and Franzolin E. (2016) Melting
720 relations in the system $\text{FeCO}_3\text{-MgCO}_3$ and thermodynamic modelling of Fe-Mg
721 carbonate melts. *Contrib. Mineral. Petrol.* **171**, 1-16.
- 722 Kang N., Schmidt M. W., Poli S., Franzolin E. and Connolly J. A. D. (2015) Melting of
723 siderite to 20 GPa and thermodynamic properties of FeCO_3 -melt. *Chem. Geol.* **400**,
724 34-43.
- 725 Katsura T. and Ito E. (1990) Melting and subsolidus phase relations in the $\text{MgSiO}_3\text{-}$
726 MgCO_3 system at high pressures: implications to evolution of the Earth's atmosphere.
727 *Earth Planet. Sci. Lett.* **99**, 110-117.
- 728 Keshav S. and Gudfinnsson G. H. (2013) Silicate liquid-carbonatite liquid transition
729 along the melting curve of model, vapor-saturated peridotite in the system CaO-

- 730 MgO-Al₂O₃-SiO₂-CO₂ from 1.1 to 2 GPa. *J. Geophys. Res.* **118**, 3341-3353.
- 731 Königsberger E., Königsberger L. C. and Gamsjäger H. (1999) Low-temperature
732 thermodynamic model for the system Na₂CO₃-MgCO₃-CaCO₃-H₂O. *Geochim.*
733 *Cosmochim. Acta* **63**, 3105-3119.
- 734 Li Z. Y., Li J., Lange R., Liu J. C. and Militzer B. (2017) Determination of calcium
735 carbonate and sodium carbonate melting curves up to Earth's transition zone
736 pressures with implications for the deep carbon cycle. *Earth Planet. Sci. Lett.* **457**,
737 395-402.
- 738 Litasov K., Shatskiy A., Podborodnikov I. and Arefiev, A. (2020) Phase diagrams of
739 carbonate materials at high pressures, with implications for melting and carbon
740 cycling in the deep earth. *Carbon in Earth's Interior, Geophysical Monograph*
741 **249**,137-165.
- 742 Liu X. and O'Neill H. S. C. (2004) The effect of Cr₂O₃ on the partial melting of spinel
743 lherzolite in the system CaO-MgO-Al₂O₃-SiO₂-Cr₂O₃ at 1·1 GPa. *J. Petrol.* **45**,
744 2261-2286.
- 745 Luth R. W. (2001) Experimental determination of the reaction aragonite+magnesite=
746 dolomite at 5 to 9 GPa. *Contrib. Mineral. Petrol.* **141**, 222-232.
- 747 Luth R.W. (2006) Experimental study of the CaMgSi₂O₆-CO₂ system at 3-8 GPa.
748 *Contrib. Mineral. Petrol.* **151**, 141-157.
- 749 Mitchell R. H. (2005) Carbonatites and carbonatites and carbonatites. *Can. Mineral.* **43**,

750 2049-2068.

751 Müller J., Müller M. K., Rhede D., Wilke F. D. H. and Wirth R. (2017) Melting relations
752 in the system CaCO₃-MgCO₃ at 6 GPa. *Am. Mineral.* **102**, 2440-2449.

753 Novella D., Keshav S., Gudfinnsson G. H. and Ghosh S. (2014) Melting phase relations
754 of model carbonated peridotite from 2 to 3 GPa in the system CaO-MgO-Al₂O₃-
755 SiO₂-CO₂ and further indication of possible unmixing between carbonatite and
756 silicate liquids. *J. Geophys. Res.* **119**, 2780-2800.

757 Pintér Z., Foley S.F., Yaxley G.M., Rosenthal A., Rapp R.P., Lanati A.W. and Rushmer,
758 T. (2021) Experimental investigation of the composition of incipient melts in upper
759 mantle peridotites in the presence of CO₂ and H₂O. *Lithos*, **396-397**, 106224.

760 Poli S. (2015) Carbon mobilized at shallow depths in subduction zones by carbonatitic
761 liquids. *Nature Geoscience* **8**, 633-636.

762 Poli S., Franzolin E., Fumagalli P. and Crottini A. (2009) The transport of carbon and
763 hydrogen in subducted oceanic crust: An experimental study to 5 GPa. *Earth Planet.*
764 *Sci. Lett.*, **278**(3-4), 350-360.

765 Rohrbach A. and Schmidt M. W. (2011) Redox freezing and melting in the Earth's deep
766 mantle resulting from carbon-iron redox coupling. *Nature* **472**, 209-212.

767 Russell J.K., Porritt L.A., Lavallee Y. and Dingwell D.B. (2012) Kimberlite ascent by
768 assimilation-fuelled buoyancy. *Nature*, **481**, 352-356.

769 Shatskiy A., Podborodnikov I. V., Arefiev A. V., Minin D. A., Chanyshv A. D. and

770 Litasov K. D. (2018) Revision of the CaCO₃-MgCO₃ phase diagram at 3 and 6 GPa.
771 *Am. Mineral.* **103**, 441-452.

772 Shatskiy A., Bekhtenova A., Podborodnikov I.V., Arefiev A.V. and Litasov, K. D. (2022)
773 Towards composition of carbonatite melts in peridotitic mantle. *Earth Planet. Sci.*
774 *Lett.* **581**, 117395.

775 Sieber M.J., Wilke F. and Koch- Müller M. (2020) Partition coefficients of trace
776 elements between carbonates and melt and suprasolidus phase relation of Ca-Mg-
777 carbonates at 6 GPa. *Am. Mineral.* **105**, 922-931.

778 Solopova N. A., Dubrovinsky L., Spivak A. V., Litvin Y. A. and Dubrovinskaia, N.
779 (2015) Melting and decomposition of MgCO₃ at pressures up to 84 GPa. *Phys. Chem.*
780 *Miner.* **42**, 73-81.

781 Spivak A. V., Litvin Y. A., Ovsyannikov S. V., Dubrovinskaia N. A. and Dubrovinsky
782 L. S. (2012) Stability and breakdown of Ca¹³CO₃ melt associated with formation of
783 ¹³C-diamond in static high pressure experiments up to 43 GPa and 3900 K. *J. Solid*
784 *State Chem.* 191, 102-106.

785 Stagno V., Ojwang D.O., McCammon C.A., Frost D.J. (2013) The oxidation state of
786 the mantle and the extraction of carbon from Earth's interior. *Nature*, **493**, 84-88.

787 Stamm N. and Schmidt M.W. (2017) Asthenospheric kimberlites: volatile contents and
788 bulk compositions at 7 GPa. *Earth Planet. Sci. Lett.* **474**, 309-321.

789 Suito K., Namba J., Horikawa T., Taniguchi Y., Sakurai N., Kobayashi M., Onodera A.

- 790 Shimomura O, and Kikegawa T. (2001) Phase relations of CaCO₃ at high pressure
791 and high temperature. *Am. Mineral.* **86**, 997-1002.
- 792 Tao R., Fei Y. and Zhang L. (2013) Experimental determination of siderite stability at
793 high pressure. *Am. Mineral.* **98**, 1565-1572.
- 794 Timmerman S., Spivak A. V. and Jones A. P. (2021) Carbonatitic melts and their role in
795 diamond formation in the deep Earth. *Elements*, **17**, 321-326.
- 796 Weidendorfer D., Schmidt M. W. and Mattsson, H. B. (2017) A common origin of
797 carbonatite magmas. *Geology* **45**, 507-510.
- 798 Weidendorfer D., Manning C. E. and Schmidt, M. W. (2020) Carbonate melts in the
799 hydrous upper mantle. *Contrib. Mineral. Petrol.*, **175**, 1-17.
- 800 Will T. M. (1998) *Phase equilibria in metamorphic rocks: Thermodynamic background*
801 *and petrological applications*. Lecture Notes in Earth Science, Vol. 71. Berlin
802 Springer.
- 803 Wyllie P. J. and Huang W. (1975) Peridotite, kimberlite, and carbonatite explained in
804 the system CaO-MgO-SiO₂-CO₂. *Geology* **3**, 621-624.
- 805 Wyllie P. J. and Huang W. (1976) Carbonation and melting reactions in the system CaO-
806 MgO-SiO₂-CO₂ at mantle pressures with geophysical and petrological applications.
807 *Contrib. Mineral. Petrol.* **54**, 79-107.
- 808 Yaxley G. M. and Brey G. P. (2004) Phase relations of carbonate-bearing eclogite
809 assemblages from 2.5 to 5.5 GPa: implications for petrogenesis of carbonatites.

- 810 *Contrib. Mineral. Petrol.* **146**, 606-619.
- 811 Yaxley G. M., Anenburg M., Tappe S., Decree S. and Guzmics T. (2022) Carbonatites:
812 Classification, Sources, Evolution, and Emplacement. *Annual Review of Earth and*
813 *Planetary Sciences*, **50**, 261-293.
- 814 Zedgenizov D. A., Shatskiy A., Ragozin A. L., Kagi H. and Shatsky V. S. (2014)
815 Merwinite in diamond from São Luis, Brazil: A new mineral of the Ca-rich mantle
816 environment. *Am. Mineral.* **99**, 547-550.
- 817 Zhao S. T., Schettino E., Merlini M. and Poli S. (2019) The stability and melting of
818 aragonite: An experimental and thermodynamic model for carbonated eclogites in
819 the mantle. *Lithos* **324-325**, 105-114.

820 **Table 1**

821 Experimental run conditions and run products determined by electron microprobe

822 analyses in the system CaCO₃ - MgCO₃. Cc_{ss}: Ca-carbonate, calcite-dolomite solid823 solution. Mag_{ss}: magnesite solid solution;

Sample #	P (GPa)	T (°C)	Run time (hrs)	Bulk X _{Ca} (mol.%)	Run products	Cc _{ss} X _{Ca}	Mag _{ss} X _{Ca}	Liq X _{Ca}
CCMS11a	3.0	1150	48	0.8	Cc _{ss}	0.80	-	-
CCMS11b	3.0	1150	48	0.7	Cc _{ss}	0.70	-	-
CCMS12a	3.0	1175	48	0.8	Cc _{ss}	0.82±0.01	-	-
CCMS12b	3.0	1175	48	0.7	Cc _{ss}	0.71±0.01	-	-
CCMS13a	3.0	1175	43	0.8	Cc _{ss}	0.81±0.01	-	-
CCMS13b	3.0	1175	43	0.7	Cc _{ss}	0.71±0.01	-	-
CCMS9a	3.0	1200	48	0.8	Cc _{ss} + Liq	0.84±0.05	-	0.79±0.04
CCMS14a	3.0	1200	48	0.75	Cc _{ss} + Liq	0.84±0.01	-	0.73±0.05
CCMS16a	3.0	1200	64	0.7	Cc _{ss}	0.71±0.01	-	-
CCMS16b	3.0	1200	64	0.65	Cc _{ss} + Liq	0.69±0.03	-	0.65±0.04
CCMS9b	3.0	1200	48	0.6	Cc _{ss} + Liq	0.64±0.04	-	0.70±0.06
CCMS14b	3.0	1200	48	0.4	Cc _{ss} + Mag _{ss}	0.45±0.01	0.10±0.01	-
CCMS17a	3.0	1225	48	0.7	Cc _{ss} + Liq	0.82±0.01	-	0.71±0.06
CCMS17b	3.0	1225	48	0.4	Mag _{ss} + Liq	0.14±0.01	-	0.59±0.03
P10-026	3.0	1230	12	0.6	Mag _{ss} + Liq			
CCMS8a	3.0	1250	47	0.8	Cc _{ss} + Liq	0.92±0.01	-	0.80±0.03
CCMS8b	3.0	1250	47	0.7	Liq	-	-	0.70±0.02
CCMS7a	3.0	1250	50	0.6	Liq	-	-	0.65±0.11
CCMS7b	3.0	1250	50	0.4	Mag _{ss} + Liq	0.12±0.01	-	0.59±0.04
CCMS10a	3.0	1300	47	0.9	Cc _{ss} + Liq	0.93±0.01	-	0.80±0.03
CCMS10b	3.0	1300	47	0.3	Liq	-	-	0.32±0.2
CCMS6a	3.0	1350	1.7	0.65	Liq	-	-	0.65
CCMS6b	3.0	1350	1.7	0.5	Liq	-	-	0.5

CCMS26a	3.0	1500	43	0.2	Liq	-	-	0.2
CCMS26b	3.0	1500	43	0.1	Liq			0.1
CCMS37a	4.5	1250	66	0.75	Cc _{ss}	0.76±0.01	-	-
CCMS37b	4.5	1250	66	0.6	Cc _{ss}	0.60±0.01	-	-
CCMS38a	4.5	1275	48	0.7	Cc _{ss} + Liq	0.80±0.02	-	0.70±0.02
CCMS38b	4.5	1275	48	0.6	Liq	-	-	0.60
CCMS36a	4.5	1300	40	0.7	Liq	-	-	0.71±0.01
CCMS36b	4.5	1300	40	0.6	Liq	-	-	0.59±0.03
1551a	6.0	1750	0.3	1.0	Liq	-	-	1.0
1551b	6.0	1750	0.3	0.0	Liq	-	-	0.0
1586a	12.0	1850	0.2	1.0	Cc _{ss}	1.0	-	-
1586b	12.0	1850	0.2	0.0	Mag _{ss}	-	0.0	-
1639	12.0	1850	0.1	0.0	Mag _{ss}	-	0.0	-
1647	12.0	1900	0.1	0.0	Mag _{ss}	-	0.0	-
1625	12.0	1950	0.1	1.0	Liq	-	-	1.0
1652	12.0	1950	0.1	0.0	Mag _{ss} + Liq	-	0.0	0.0
1627	12.0	2000	0.1	1.0	Liq	0.0	-	-

825 **Table 2**826 Standard molar thermodynamic properties of aragonite, calcite V, magnesite, liquid MgCO₃, liquid CaCO₃ at 298.15 K and 1 bar.827 G_0 Gibbs free energy; S_0 entropy; V_0 volume; c_1 - c_5 coefficients for heat capacity polynomial; α_0 thermal expansivity; K_0 bulk modulus; K' pressure828 derivative of the bulk modulus. Parameter b_7 equals $K_0 \times B$ (see eq. 8 in text), as used in Perplex (Connolly 2005, 2009).

829

Phase	G_0 (J)	S_0 (J/K)	V_0 (J/bar)	α_0 (1/K)	K_0 (bar)	b_7	K'
Aragonite	-1234014	87.99	3.395	1.08E-4	689960	-103.49	4.397
Calcite V	-1234130	93.783	3.6	1.10E-4	725200	-108.78	4
Magnesite	-1130439	65.5	2.79	7.04E-5	1080000	-162	5
Liquid MgCO ₃	-1056600	99.221	3.5	2.35E-4	100000	-34.27	6.637
Liquid CaCO ₃	-1185900	97.175	3.75	2.35E-4	307286	-94.86	4

$$C_p = c_1 + c_2 \times T + \frac{c_3}{T^2} + c_4 \times T^2 + \frac{c_5}{\sqrt{T}}$$

Phase	C_1	C_2	C_3	C_4	C_5
Aragonite	183.423	5.46770E-3	755.626E3	0	-1927.66
Calcite V	202.857	4.16519E-3	1937.2E3	0	-2463.64
Magnesite	185.4	-2.83E-3	24.502E3	0	-1877.0
Liquid MgCO ₃	101.814	2.658E-2	-194.019E3	-6.298E-6	325.39
Liquid CaCO ₃	165.269	1.400E-2	100.562E4	0	-936.792

830

831 **Table 3**

832 Fitted interaction parameter w_{ij} in J/mol for melt solution model of the system

833 $CaCO_3^{liquid}$ (ccL) - $MgCO_3^{liquid}$ (magL), without and with the third intermediate

834 component $Ca_{0.5}Mg_{0.5}CO_3^{liquid}$ (dolL).

835

Interaction parameter	Two-component model			Three-component model		
	w_{ij}^H	w_{ij}^S	w_{ij}^V	w_{ij}^H	w_{ij}^S	w_{ij}^V
	(J/mol)	(J/mol)	(J/mol)	(J/mol)	(J/mol)	(J/mol)
ccL - magL	35E3	0	-1.10	-5E3	30.	1.15
magL - ccL	-110E3	0	0.20	-100E3	0	0.30
magL - dolL	-	-	-	-25E3	0	-0.40
ccL - dolL	-	-	-	-30E3	0	-0.20
dolL - magL	-	-	-	-5E3	0	-0.80
dolL - ccL	-	-	-	-30E3	0	-0.30

836 w_{ij}^H - enthalpic, w_{ij}^S - entropic, w_{ij}^V - volumetric terms of the interaction parameters

837 w_{ij} . cc - calcite, mag - magnesite, dol - dolomite, L - liquid.

838 **Figure Captions**

839 **Figure 1.** P-T diagram compiling experiments in the system CaCO₃ (a) and MgCO₃ (b)
840 showing calculated phase relationships after thermodynamic analysis performed in this
841 study. a) open red symbols refer to the presence of liquid CaCO₃, solid symbols to
842 subsolidus run products; crosses stand for experiments performed in this study, circles
843 are from Irving and Wyllie (1975), triangles from Shatskiy et al. (2018), stars are Pt-
844 sphere marker experiments from Li et al. (2017), diamonds conductivity experiments
845 from Li et al. (2017), six-corner stars from Suito et al. (2001), squares from Zhao et al.
846 (2019), polygon is from Spivak et al. (2012); b) open red symbols stand for the presence
847 of liquid MgCO₃, solid black symbols for magnesite, grey symbols for the occurrence
848 of periclase; circles are from Irving and Wyllie (1975), triangles from Shatskiy et al.
849 (2018), large triangles from Müller et al. (2017), stars from Katsura and Ito (1990),
850 diamonds from Solopova et al. (2015).

851 **Figure 2.** Isobaric T-X (temperature-composition) diagrams in the CaCO₃-MgCO₃
852 binary at a) 1.0 GPa, after Byrnes and Wyllie (1981); b) 2.7 GPa, blue line after Irving
853 and Wyllie (1975), and 3.0 GPa, magenta line after Shatskiy et al. (2018); c) 6.0 GPa,
854 green after Buob et al. (2006), brown after Müller et al. (2017), and magenta after
855 Shatskiy et al. (2018); Abbreviations: C = calcite, D = dolomite, A = aragonite, Pe =
856 periclase, M = magnesite, L = Liquid, V = CO₂ vapor. The bold bars at the bottom of
857 the figure give the range of X_{Ca} for the minimum as permitted by the individual
858 experiments of each data set.

859 **Figure 3.** Representative Back-scattered electron (BSE) images of cross sections of the
860 recovered capsules at 3.0 showing sub-solidus, near-solidus and super-solidus
861 conditions. a) run charges ccms11a, b at 1150 °C, and X_{Ca} 0.7 and 0.8; b) run ccms14b
862 displays the subsolidus assemblage magnesite + dolomite at 1200 °C, on the Mg-rich
863 side of the binary; c) run ccms16, 1200 °C, the capsule at the bottom in figure shows
864 subsolidus, polygonal Mg-calcite at $X_{Ca} = 0.7$, and the other capsule solid + liquid at
865 $X_{Ca} = 0.65$, d) superliquidus run ccms8b, at 1250 °C, $X_{Ca} = 0.7$.

866 **Figure 4.** Isobaric T-X phases diagrams in the $CaCO_3$ - $MgCO_3$ system showing
867 experimental results at 3 GPa and 4.5 GPa. Black circles stand for the composition of
868 carbonate, open red circles for estimated liquid composition coexisting with a carbonate,
869 solid red circles are superliquidus experiments.

870 **Figure 5.** Compression curves for $MgCO_3^{liquid}$ (blue) and $CaCO_3^{liquid}$ (orange) at
871 1100 K after Hurt and Wolf (2020), compared to molar volumes at selected pressures
872 (circles) calculated using the equation of state retrieved in this study. Dashed line stands
873 for the model of $MgCO_3^{liquid}$ obtained by molecular dynamics, whereas solid lines
874 represent the compression curve for 6-fold metal carbon coordination.

875 **Figure 6.** Isobaric T-XMg phase diagram calculated using a two-component liquid
876 model at 3 GPa (a) and 6 GPa (b). Red dots at 3 GPa stand for liquid compositions in
877 experiments of this study, at 6 GPa of Müller et al. (2017). Black dots are compositions
878 of carbonates coexisting with liquids in these studies.

879 **Figure 7.** Phase diagrams using the solution model including a $Ca_{0.5}Mg_{0.5}CO_3$

880 component, compared to experimental results from this study and previous studies.
881 Black dots are subsolidus or solidus experiments, red dots liquidus or superliquidus
882 experiments. Data at 1 GPa are from Byrnes and Wyllie (1981), and at 6 GPa from
883 Müller et al. (2017). Dashed lines at 6 GPa represent the phase diagram obtained
884 including aragonite, after Zhao et al. (2019).

885 **Figure 8.** Pseudosection calculated for bulk compositions used by: a) Canil and Scarfe
886 (1990), system CMS, solid black boxes stand for experimental conditions where the
887 assemblage olivine (Ol) + clinopyroxene (Cpx) + magnesite (Mag) was found, half-
888 filled red boxes stand for experiments with olivine + clinopyroxene + magnesite +
889 liquid; open red boxes for olivine + clinopyroxene + liquid; dashed line represents the
890 reaction orthopyroxene + dolomite = clinopyroxene + magnesite calculated using pure
891 diopside; b) Dalton Presnall (1998), where red open boxes are solidus experiments ; c)
892 Gudfinnsson and Presnall (2005). The solidus is highlighted as a red curve; isopleths of
893 $100 * X_{Ca}$ are in red for liquid, blue for magnesite, and green for Mg-calcite-dolomite
894 solid solutions. Opx is orthopyroxene, Gt is garnet, Sp is spinel, Cc is Mg-calcite, Dol
895 is dolomite.

896

Fig. 1

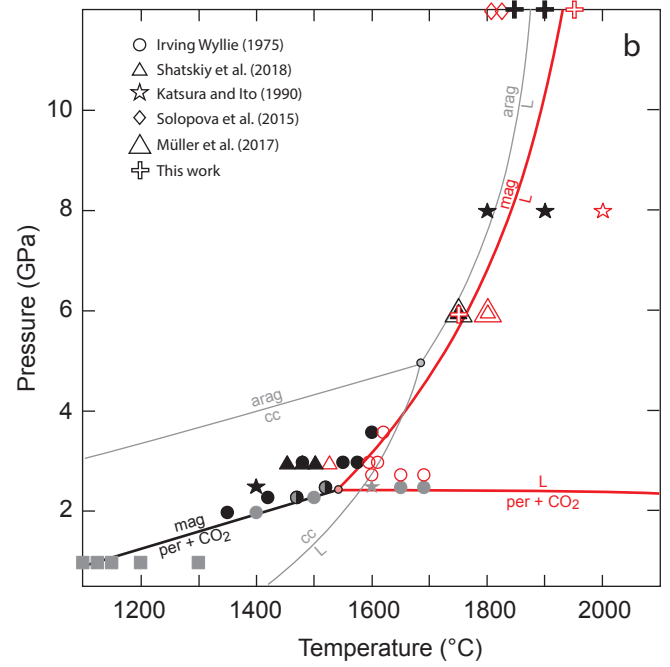
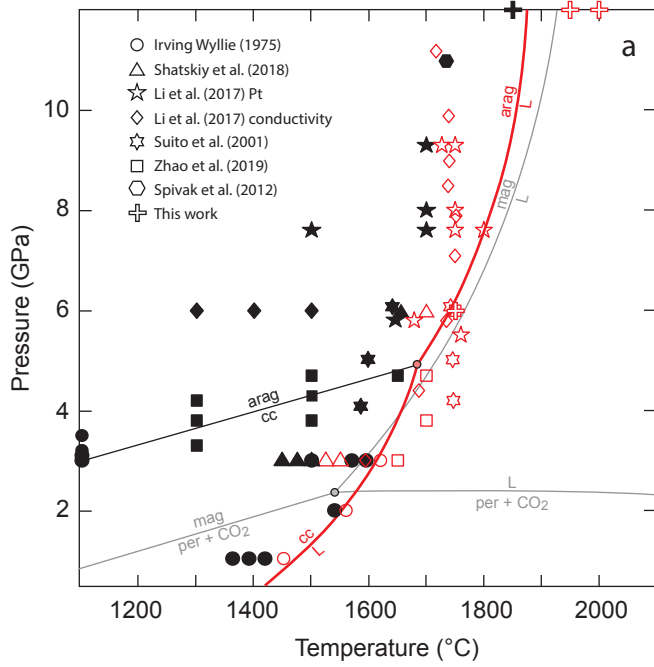


Fig 2

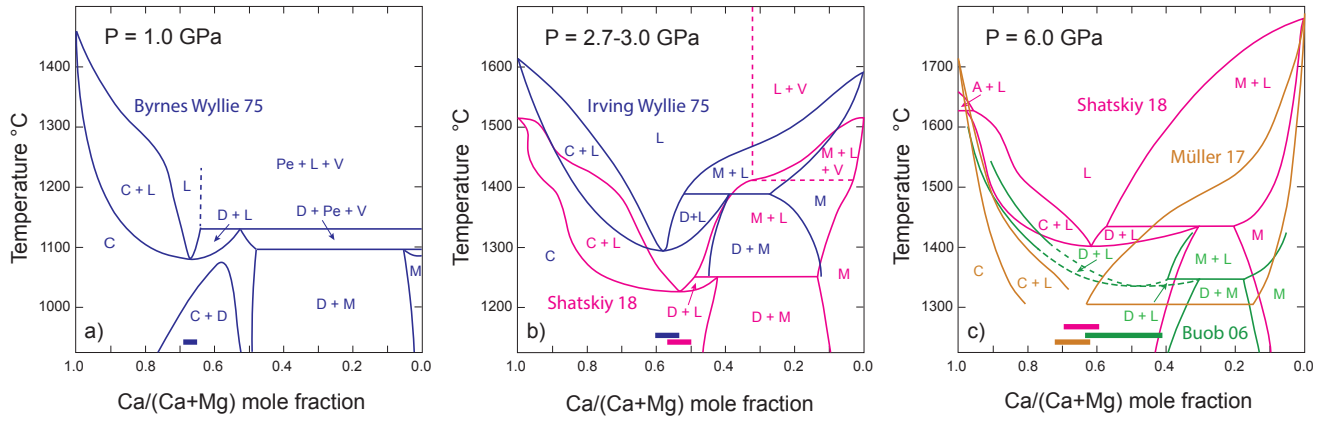


Fig. 3

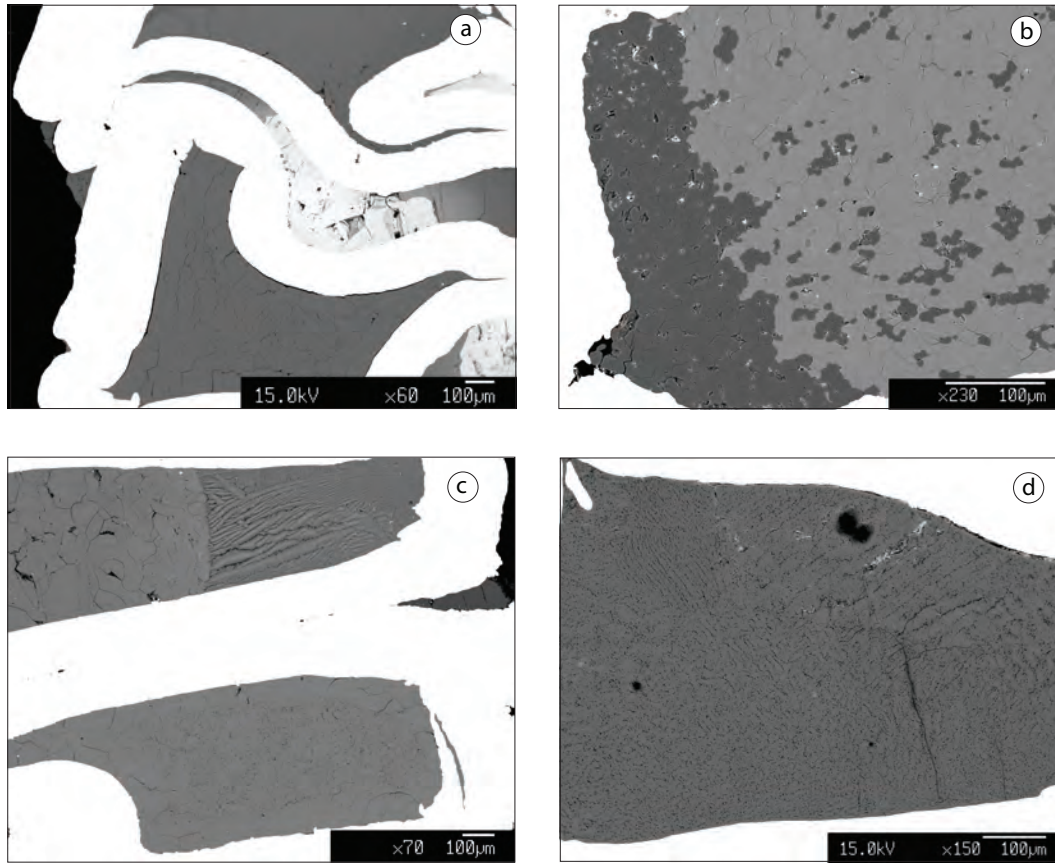


Fig. 4

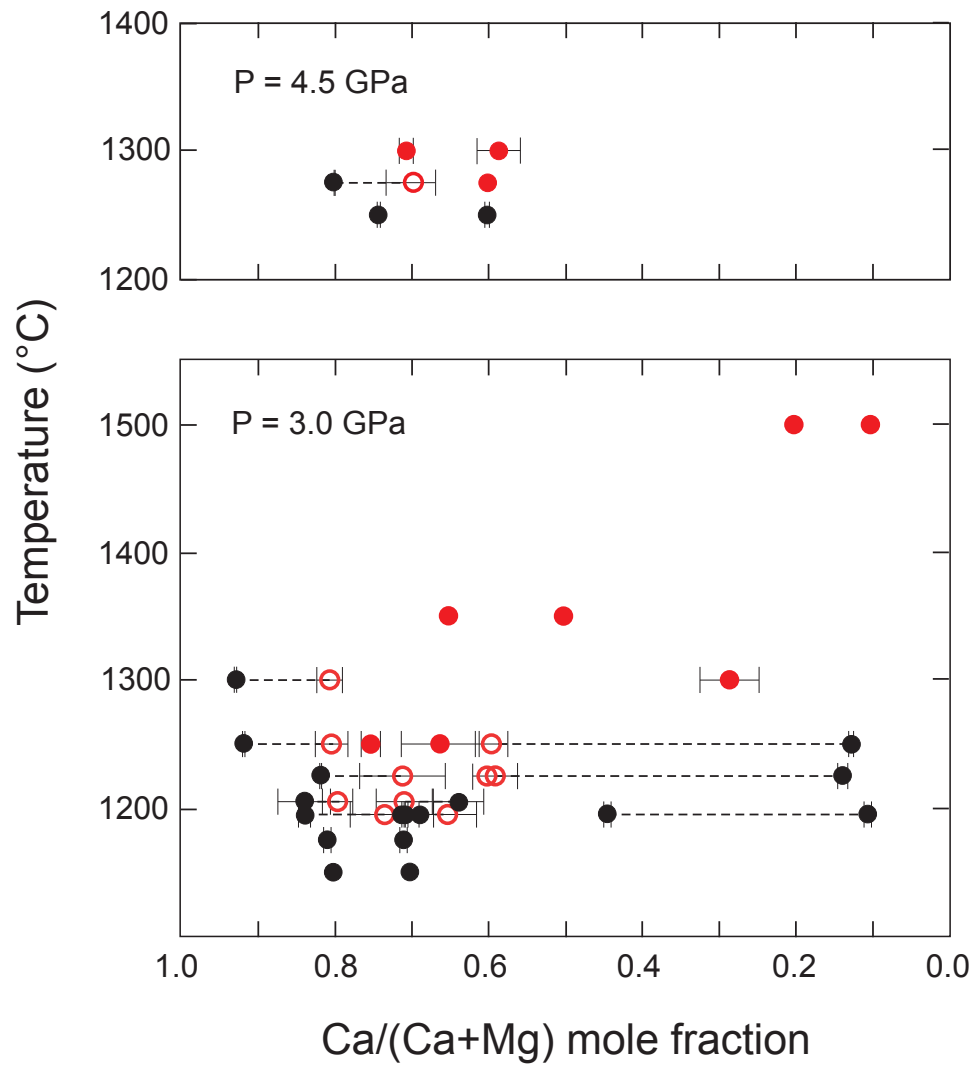


Fig. 5

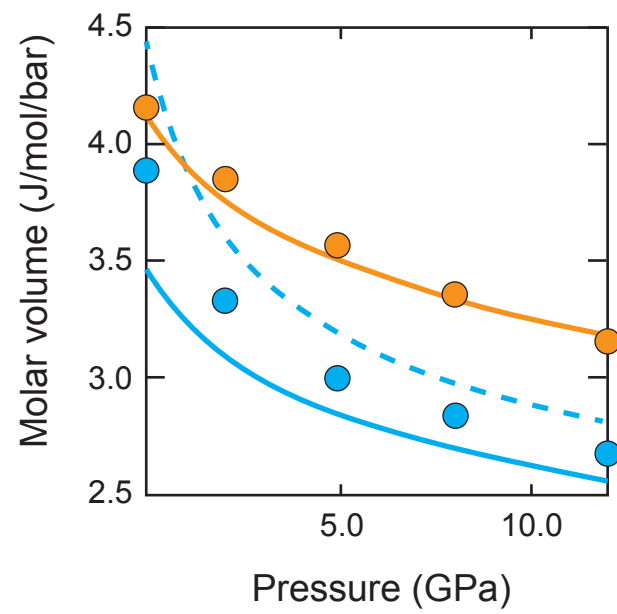


Fig. 6

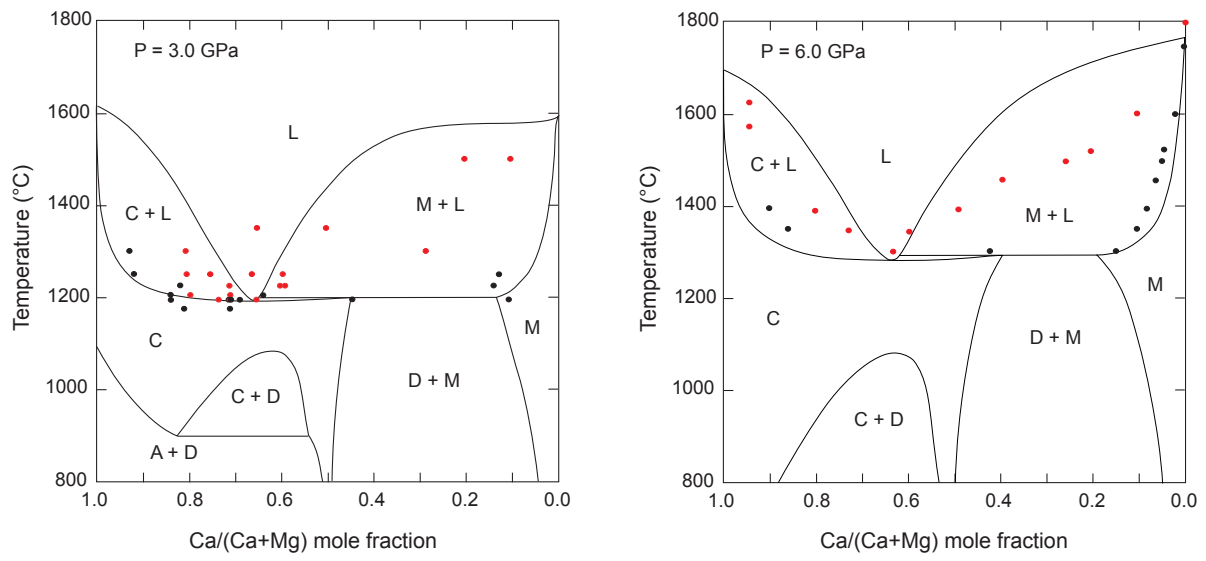
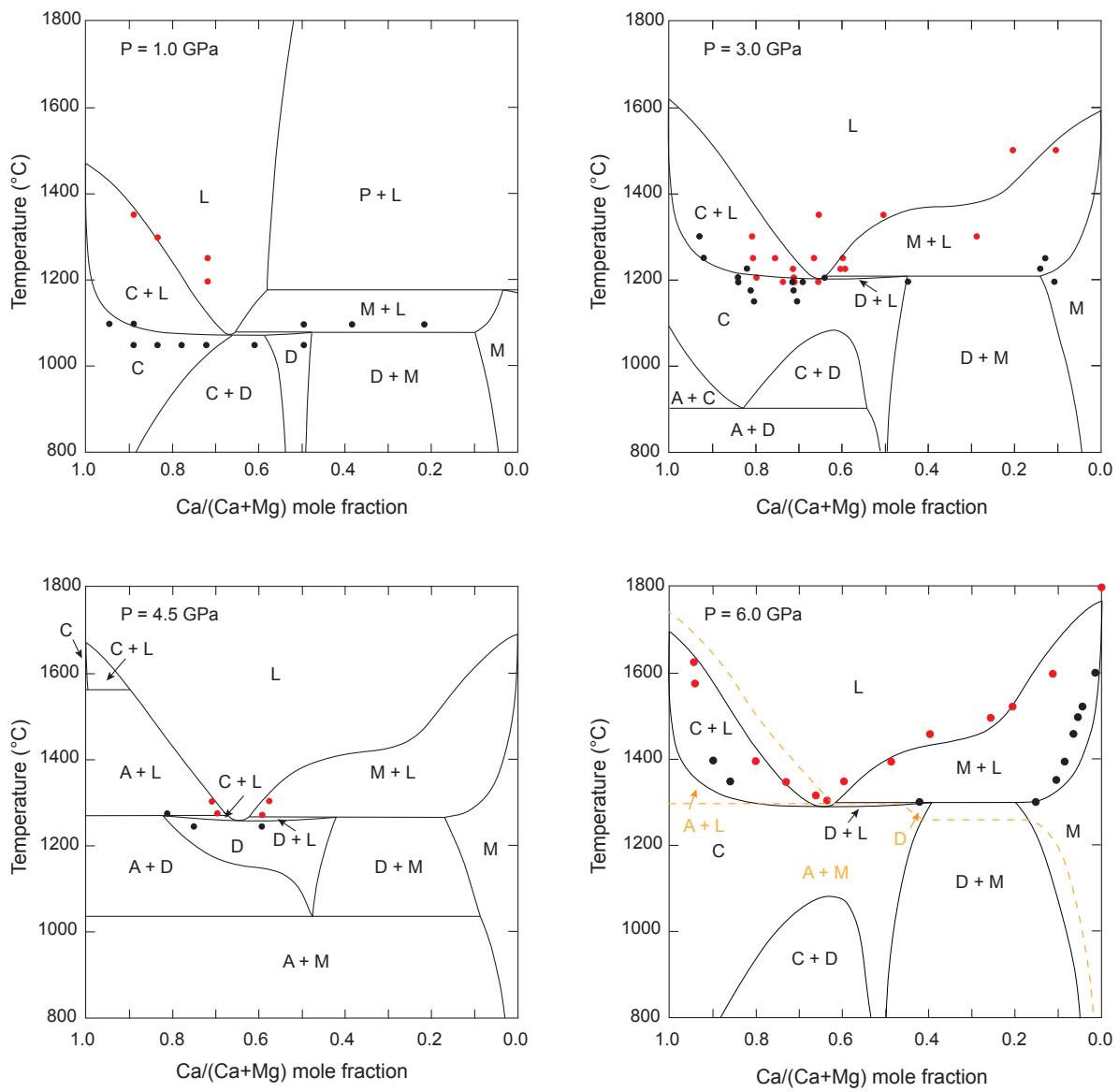


Fig. 7



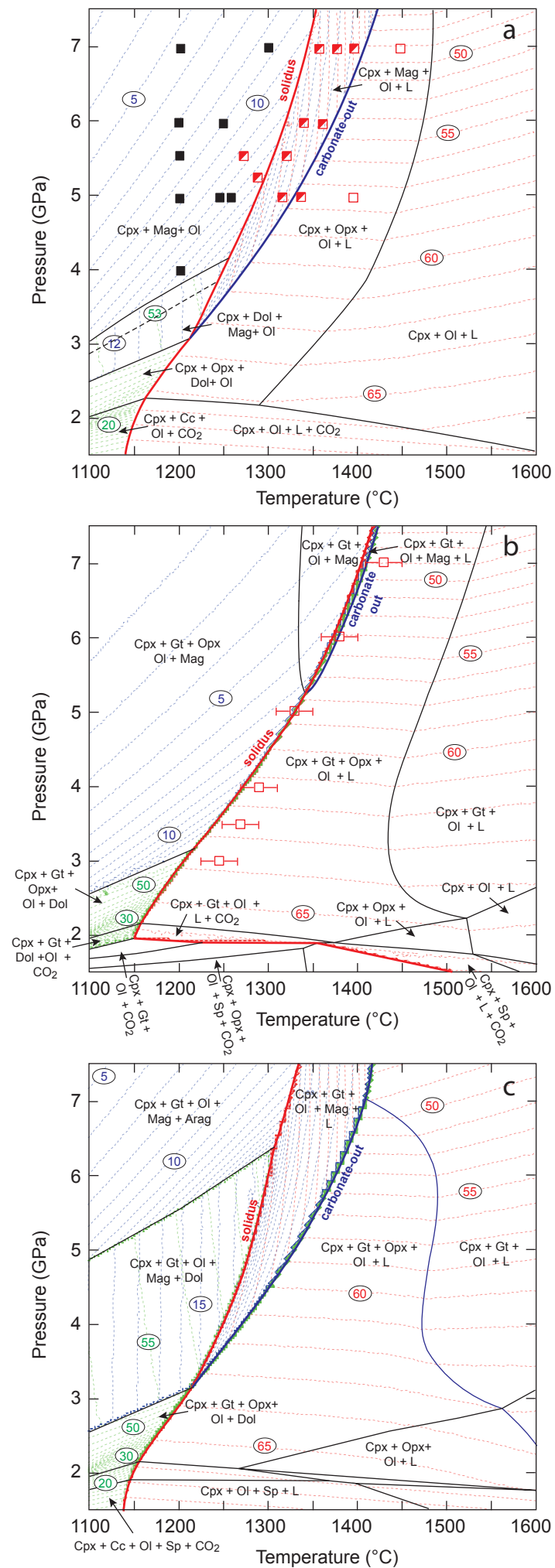
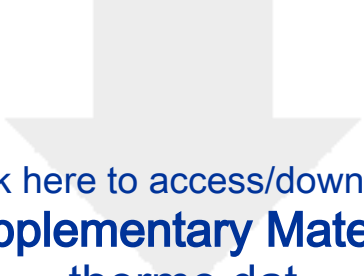


Fig. 8

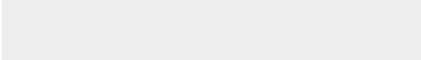



Click here to access/download
Supplementary Material
Appendix_A.pdf





Click here to access/download
Supplementary Material
thermo.dat





Click here to access/download
Supplementary Material
solution_model.dat



Declaration of interests

The authors declare that they have no known competing financial interests or personal relationships that could have appeared to influence the work reported in this paper.

The authors declare the following financial interests/personal relationships which may be considered as potential competing interests: